Numerical Modeling of No Vent Filling of a Cryogenic Tank with Thermodynamic Vent System Augmented Injector

4 authors, including:

Alok Majumdar
NASA
102 PUBLICATIONS **1,009** CITATIONS
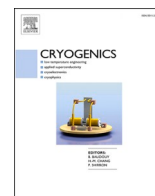
SEE PROFILE

Jason Hartwig
NASA
158 PUBLICATIONS **1,463** CITATIONS

SEE PROFILE

Numerical modeling of no vent filling of a cryogenic tank with thermodynamic vent system augmented injector

Alok Majumdar [a,d,*], Andre LeClair [a], Jason Hartwig [b], S. Mostafa Ghiaasiaan [c]

[a] *NASA Marshall Space Center, Huntsville, AL 35812, USA*
[b] *NASA/Glenn Research Center, Cleveland, OH 44135, USA*
[c] *Georgia Institute of Technology Atlanta, GA 30332-0405, USA*
[d] *Thermal Analysis Branch, NASA Marshall Space Flight Center, Huntsville, AL 35812, USA*

ABSTRACT

This paper describes a computational procedure to simulate the chilldown and No Vent Filling of a cryogenic tank with a Thermodynamic Vent System (TVS) assisted injector. During No Vent Filling with a TVS augmented injector, the cryogenic liquid coming from a supply tank is divided into two streams prior to entering the target tank; a small portion of the liquid is allowed to pass through a Joule-Thomson valve to produce a mixture of cold liquid and vapor that is used to cool the second stream that carries the bulk of the incoming fluid before it is injected into the tank. The cold stream is also used to cool the surface of the injector, further helping to reduce the tank pressure before it exits to a vacuum. The Generalized Fluid System Simulation Program (GFSSP), a general-purpose flow network code, has been used to simulate the chill and fill process and compare with the test data. The numerical model accounts for a) different regimes of pool boiling heat transfer that occur during tank chilldown, b) condensation of vapor around spray droplets, at the interface of the cooled injector and ullage, and at the liquid–vapor interface, and c) compression of ullage vapor by the rising liquid level. The observed discrepancy between test and predictions for tank pressure is within 20% and tank filling time is within 4%.

1. Introduction

Filling a tank with cryogenic fluid is more challenging than filling a tank with water or any other fluid that is in liquid state at atmospheric condition. Filling a tank with cryogenic fluid is a two-step process. First the tank and the transfer line must be chilled. Liquid cryogens start flowing into the tank only after the tank and transfer lines are chilled to the fluid saturation temperature. In normal gravity, cryogenic tanks are usually filled from the bottom at nearly atmospheric pressure. The vapor, caused by heat transfer from the warm tank walls, is allowed to vent from the top of the tank while the tank is being filled. Filling a cryogenic tank in the absence of gravity is more challenging because in a non-stratified environment liquid propellant may not settle at the tank bottom as it does on earth. There is a strong possibility that liquid propellant may exit through the vent valve, which is typically located at the top of the tank to vent propellant vapor. There are several methods of filling a tank in space.

To reduce the loss of precious propellant, a "charge-hold-vent" (CHV) method of tank filling [1] was developed. During the charge period, a small quantity of liquid cryogen is injected into the evacuated tank. Initially, the liquid flashes due to the low tank pressure, and then the remaining liquid droplets evaporate as they contact warm vapor or the tank wall. During the hold period, the circulating flow pattern induced from the spray nozzles provides convective heat transfer from cold vapor to the tank wall. The primary mode of heat transfer during the hold is convection. At the completion of the hold period, the pressure has risen considerably, and the tank is ready to be vented. Since venting occurs as an isentropic blowdown, some additional cooling may be recovered by stage-wise venting [2]. This method, however, proves difficult to find an optimum frequency of "charge-hold-vent" cycles and the amount of charge for each cycle.

A simpler method is that of Vented-Chill / No-Vent-Fill (VCNVF) [3]. In this method, the tank's vent valve is open for an initial period while the tank walls are chilled with a spray of cryogenic liquid that boils to vapor and exits through the vent. When the tank walls have been sufficiently chilled, the vent valve is closed, and the tank is filled with liquid. Care must be taken with the timing of the vent closure. If the vent is closed too early, residual heat in the walls may drive sufficient boil-off to raise the tank pressure high enough to stall the inlet flow. If the vent is closed too late, some liquid propellant may be lost through the vent. Compared to the CHV method, VCNVF is less mass efficient; the gas being vented during the chill may not be extracting the maximum possible thermal energy from the tank wall. There is always the risk that some of the precious liquid propellant will be vented. However, VCNVF is much simpler from an operational standpoint. The transfer lines need

Nomenclature

A	area
A_{eff}	Effective area of heat transfer
B	Laplace reference length $\left(\sqrt{\frac{\sigma}{g(\rho_f - \rho_v)}}\right)$
C_p	specific heat
D	diameter
d	bubble diameter
g	gravitational acceleration
H	heat transfer coefficient
h	enthalpy
λ	latent heat of vaporization
k	thermal conductivity
J	Mechanical Equivalent of Heat ($=778\ lb_f - ft/Btu$)
K_f	flow resistance coefficient
L	characteristic length
M	molecular weight
m	resident mass
$\dot{m}$	Mass flow rate
$\dot{m}_{cond}$	Condensation rate
Nu	Nusselt number
p	pressure
Pr	Prandtl number $\left(\frac{\mu c_p}{k}\right)$
Gr	Grashof number $\left(\frac{g\beta(T_s - T_\infty)L^3}{\nu^2}\right)$
Ra	Rayleigh number $\left(\left(\frac{L^3 \rho_v (\rho_l - \rho_v) g}{\mu_v^2}\right)\left(\frac{c_p \mu}{k}\right)_v\right)$
U	velocity
V	volume
$Q, \dot{q}$	heating rate
q''	heat flux
T	temperature

Greek

α	thermal diffusivity
δ_L	thickness of saturated layer
ϵ	porosity
μ	viscosity
ν	kinematic viscosity
ρ	density
σ	surface tension
Θ	angle between flow vector and gravity vector
$\Delta\tau$	time step

Subscript

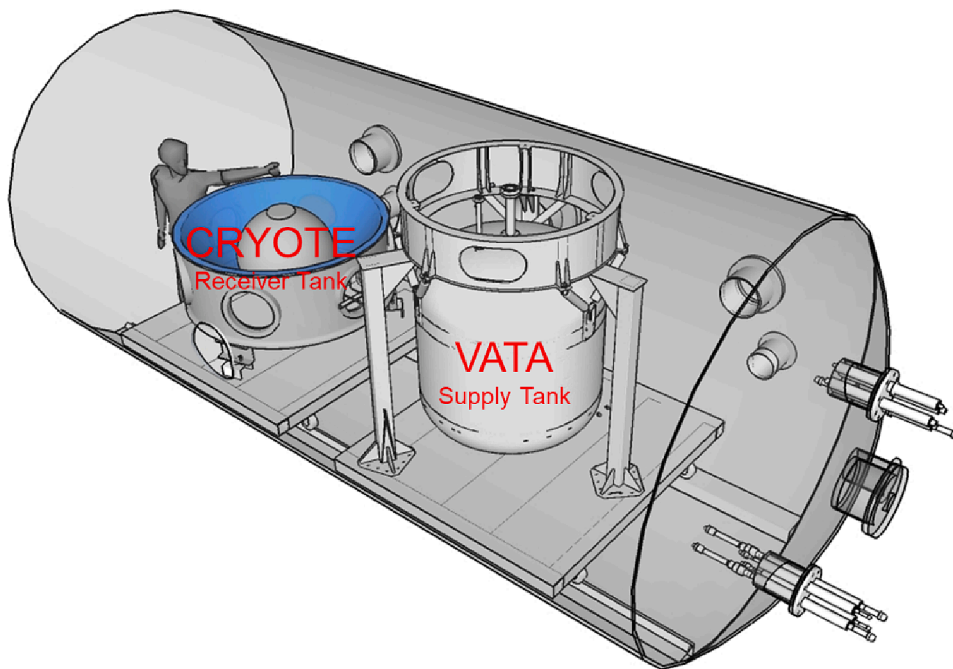|	
c	critical
CHF	critical heat flux
cond	condensation
eff	effective
f	liquid
fg	enthalpy of evaporation
FB	film boiling
v	vapor
NB	nucleate boiling
NC	natural convection
LFP	Leidenfrost point
ONB	onset nucleate boiling
S	Solid surface / Saturation
i	node
ij	branch or conductor
inj	injector
L	Liquid
t	turbulent
u	ullage
v	vapor
US	Ullage to Saturated layer
SW	Saturated Layer to Wall
W	wall

Fig. 1. CRYOTE and VATA tanks in vacuum chamber.
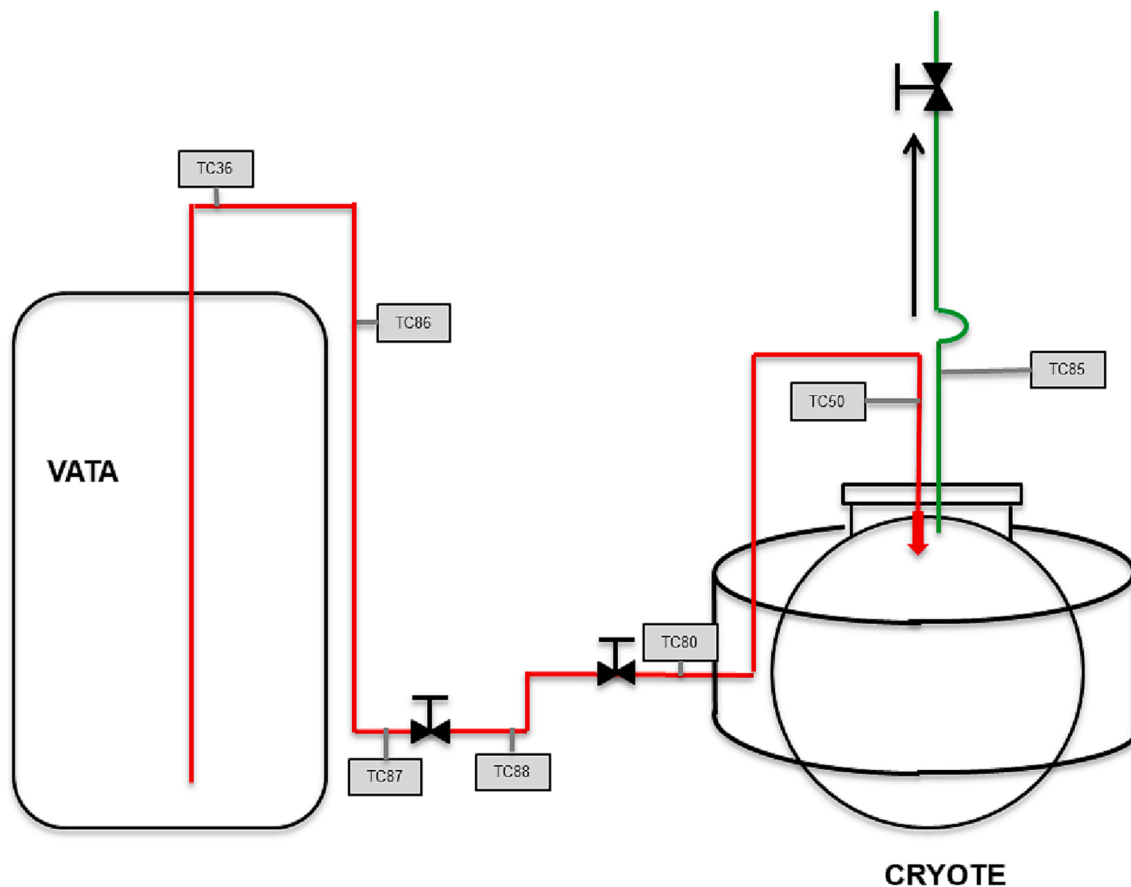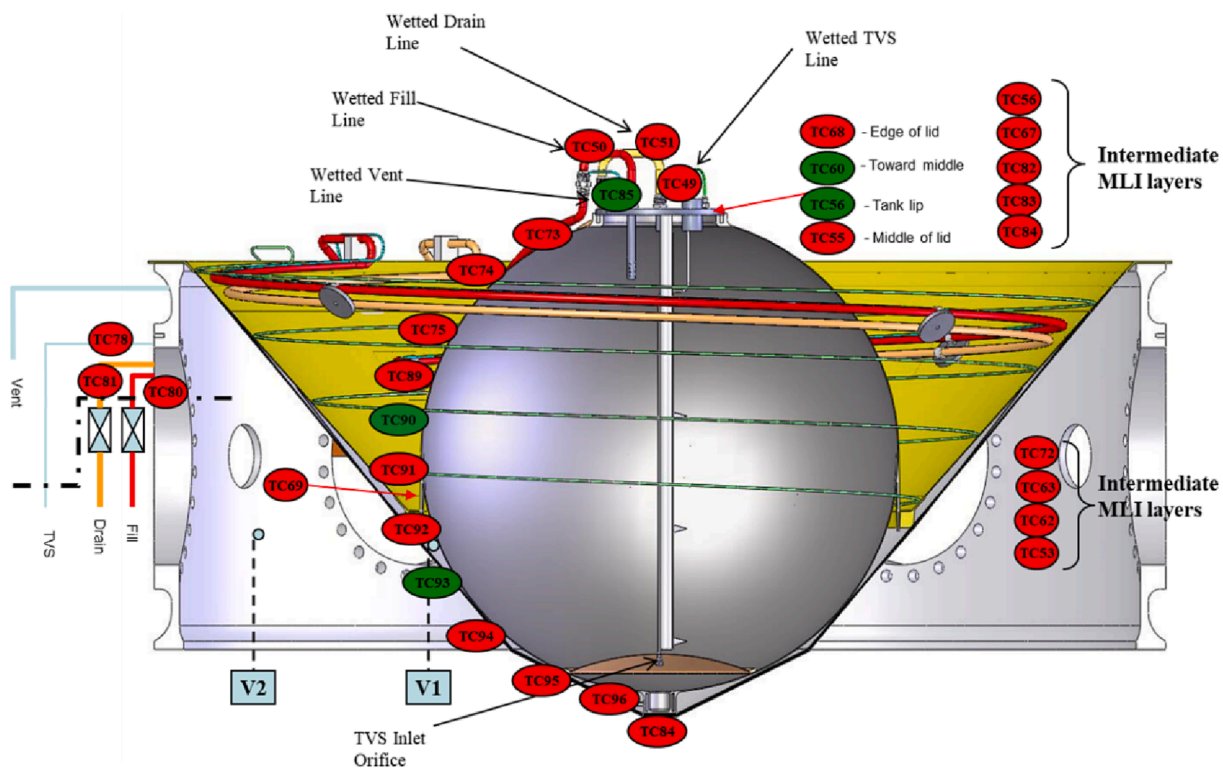
Fig. 2. Transfer and vent lines with thermocouples.

Fig. 3. CRYOTE tank instrumentation.

Fig. 4. Photograph of TVS-Augmented Injector.

Fig. 5. Modified fluid flow paths in and out of CRYOTE.

to be chilled down only once and there is less cycling of inlet and vent valves. Since there is no hold period, overall loading time is likely to be shorter.

The limitation of the VCNVF method to find an optimum target temperature was overcome by the No Vent Fill (NVF) method where a TVS (Thermodynamic Vent System) augmented injector was used with the vent valve closed during the entire filling process. NVF tests were conducted in the CRYogenic Orbital Testbed (CRYOTE) tank, which was also used for carrying out the VCNVF test. In a TVS-augmented injector, the liquid flow splits into two streams: the minor stream is routed to a Joule-Thomson (J-T) orifice where the flow immediately flashes from liquid to vapor or two phase mixture, because the downstream of the J-T leg is maintained at vacuum level; the primary stream is injected into the tank after being cooled by the cold vapor of the J-T leg in a heat exchanger. The flow through the J-T leg is also used to cool the outer metal matrix of the injector which in turn cools the vapor in the tank ullage. The cooling of vapor in the ullage by the cold injector surface reduces the ullage pressure, allowing liquid to enter and fill the tank.

Numerical modeling of Charge-Hold-Vent method and VCNVF method has been described in Refs. [6] and [16] respectively. In this paper we report on a computational method that has been developed to simulate the chill and fill process in a flight tank with a TVS augmented injector using the Generalized Fluid System Simulation Program (GFSSP), a general-purpose flow network code [4].
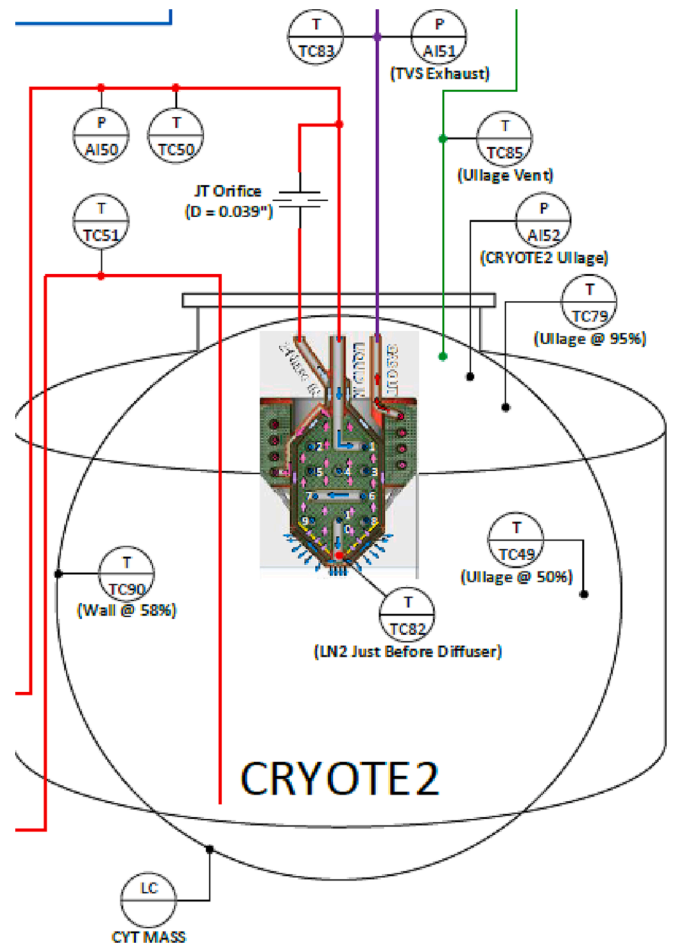
Table 1

Events in TVS-Augmented NVF Test 20180403 & 20180404.

Test 20180403		Test 20180404	
Time (sec)	Event Description	Time (sec)	Event Description
50	Pre-pressurize VATA supply tank from 101 to 379 kPa (14.7 to 55 psia)	16	Pre-pressurize VATA supply tank from 101 to 379 kPa (14.7 to 55 psia)
803	Open fill valve	1237	Open fill valve
840	TC50 suggests saturated two-phase flow entering CRYOTE	1280	TC50 suggests saturated two-phase flow entering CRYOTE
890	Peak in CRYOTE ullage pressure at 56 psia; transfer flow stalls	1351	Peak in CRYOTE ullage pressure at 58 psia; transfer flow stalls
~920–1300	Stop-Start inlet flow	~1400–1800	Stop-Start inlet flow
~1300–1400	Load cells suggest liquid accumulation begins in CRYOTE	~1760–1830	Load cells suggest liquid accumulation begins in CRYOTE
1600	TC50 suggests pure liquid flow entering CRYOTE	1872	TVS Secondary Flow turned off
2300	TVS Secondary Flow turned off	2000	TC50 suggests pure liquid flow entering CRYOTE
2710	Stop fill at 89% full	3268	Stop fill at 89% full

2. Test data

For a detailed description of the hardware and instrumentation, the reader is referred to Hartwig et al. [3], only a brief description is given
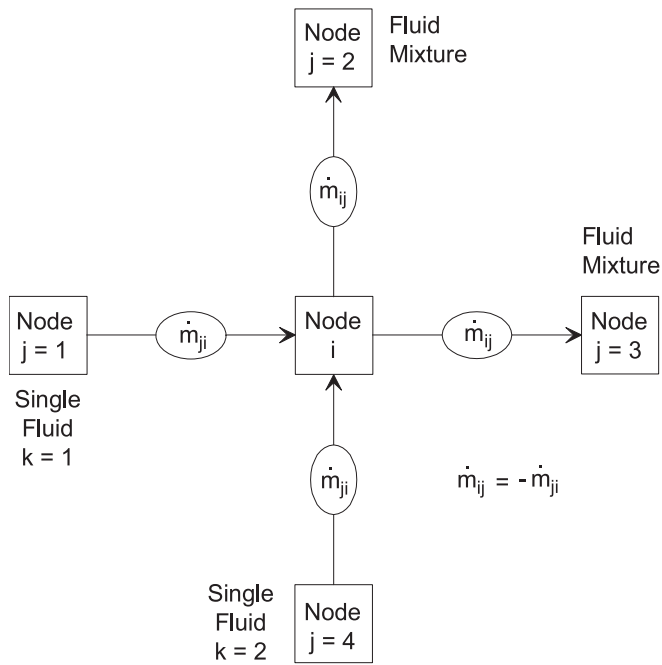
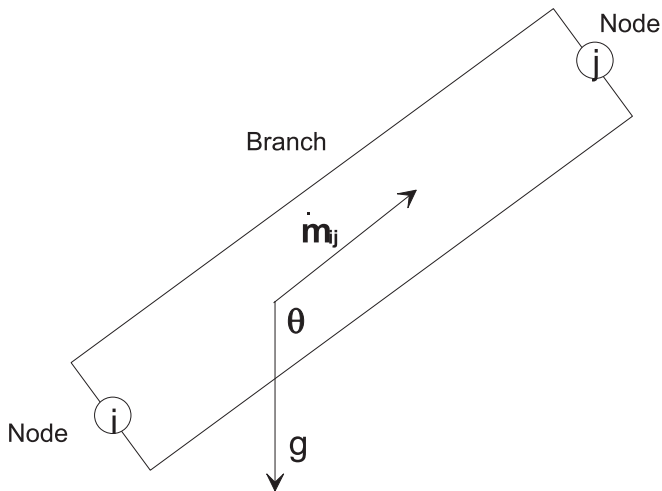**Fig. 6.** Schematic of GFSSP Nodes, Branches and Indexing Practice.

Fig. 7. Schematic of a Branch showing location of pressure, mass flowrate and gravity.

Table 2
Mathematical closure.

Variable Number	Variable Name	Designated Equation to Solve the Variable
1	Pressure	Mass Conservation
2	Flowrate	Momentum Conservation
3	Fluid Enthalpy	Energy Conservation of Fluid
4	Solid Temperature	Energy Conservation of Solid
5	Fluid Mass	Thermodynamic State

here. The tank is a 6–4 Titanium sphere with outer diameter of 29.70 inches (75.44 cm) and 0.05-inch (1.27 mm) wall thickness. To minimize heat conduction into the tank, it is mounted in a cone-shaped composite skirt. The mass of the titanium sphere is 22.7 lbm (10.28 kg), and the mass of the stainless-steel lid is 6.35 lbm (2.88 kg).

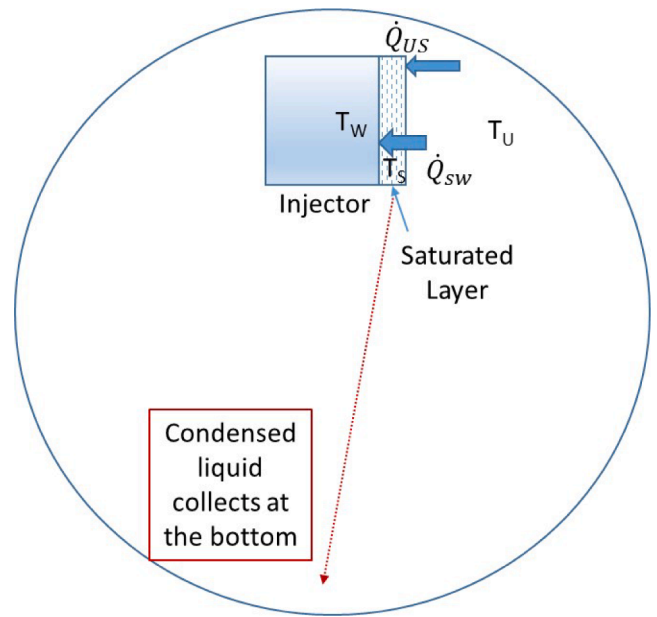To eliminate convection heat transfer, tests were carried out in a

Fig. 8. Schematic of Injector – Ullage Condensation Model.

Table 3
Injector surface geometry.

Body Metal Volume	Lattice Total Volume	Lattice Surface Area	Total Surface Area
Liter (in^3)	Liter (in^3)	m^2 (in^2)	m^2 (in^2)
0.065 (3.94)	0.27 (16.55)	0.24 (379.69)	0.22 (345.43)

vacuum chamber, as shown in Fig. 1. The larger VATA test tank was used as the supply tank for liquid nitrogen (LN2). To reduce radiation heat transfer, CRYOTE was covered with Multi-Layer Insulation (MLI). Based on earlier boil-off tests, steady-state heat leak into CRYOTE is estimated at 10 W.

The transfer line between VATA and CRYOTE is approximately 210 inches (5.33 m) of 0.5-inch (1.27 cm) outer-diameter stainless steel tubing, with a mass of 4.2 lbm (1.9 kg). There is no separate pre-chill of the transfer line: vapor created during line chilldown enters the CRYOTE tank. As shown in Fig. 2, a series of thermocouples measures the temperature of the outer wall of the pipe. TC50, located just upstream of the CRYOTE injector, is a wetted thermocouple on the inside wall of the transfer line.

Fig. 3 presents the CRYOTE tank instrumentation. Most of the thermocouples are placed on the outside wall of the tank. Green indicates that the thermocouple was tested as a possible trigger for closure of the vent valve during VCNVF tests. Not shown are TC49 and TC79, wetted thermocouples inside the tank at the 39.5% and 95% fill levels.

In addition to temperature measurements, pressure transducers measure the pressures in the ullages of VATA and CRYOTE, as well as the pressure just upstream of the CRYOTE injector. Load cells provide the mass of VATA and CRYOTE. The change in tank mass over time can be used to calculate the transfer line average flow rate; there was no liquid flow meter used in the tests. All thermocouples had +/-2 K uncertainty and the accuracy of the pressure transducers was +/-0.5 %. The details of the experiments are described by Hartwig et al [3].

With the TVS-Assisted NVF method, the tank vent can be kept closed at all times during the filling process. Fig. 4 is a photograph of the TVS-Augmented Injector. It is located about 10 cm below the top of tank.

The primary flow enters through central tube and secondary flow through J-T valve enters from the left. The LN2 is subcooled by heat transfer to the colder two-phase. The LN2 exits the bottom of the injector
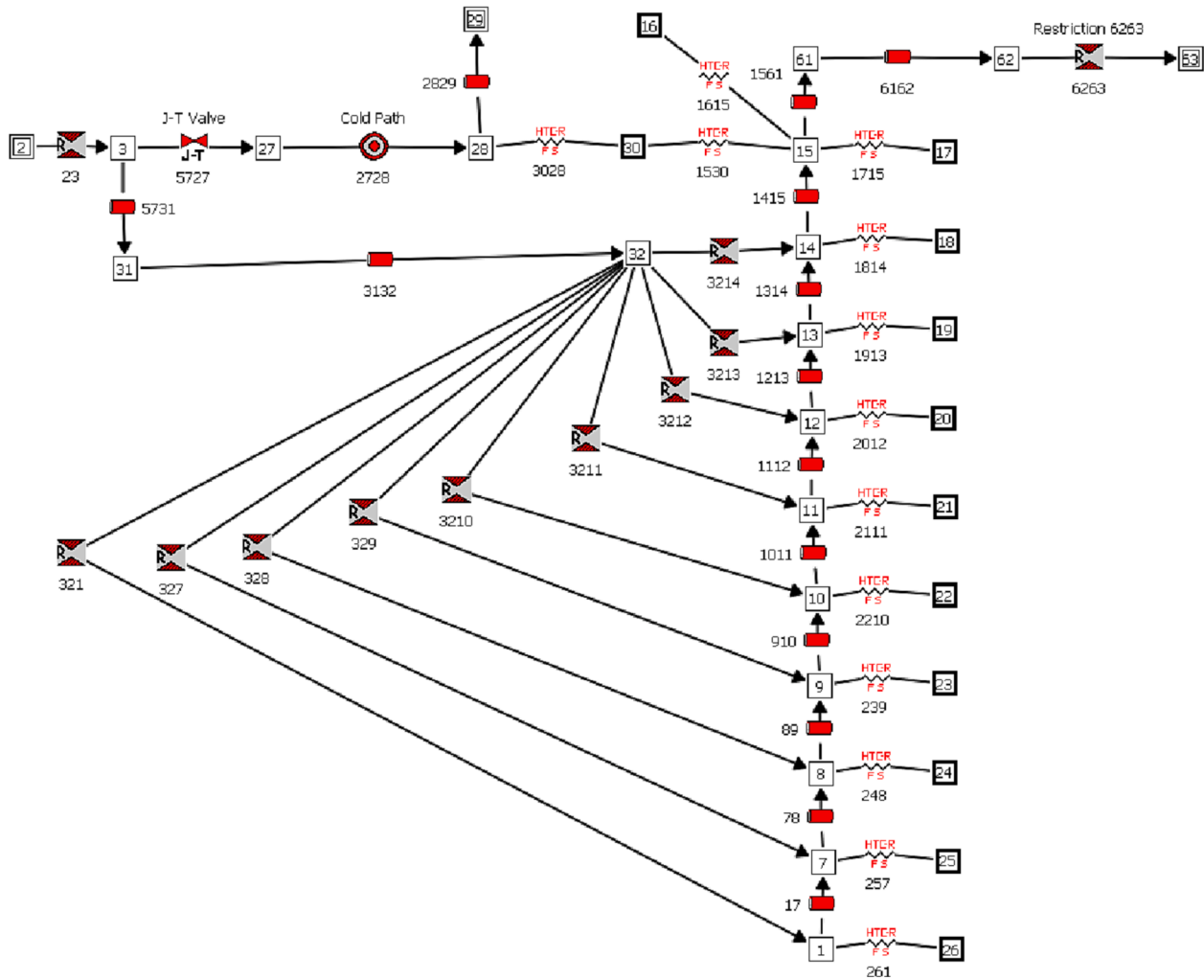
Fig. 9. GFSSP Model of CRYOTE tank with TVS assisted injecton.

and is sprayed into the tank.

After subcooling the main flow, the secondary flow follows the spiral paths at the top of the injector. The mesh design increases the heat transfer area between the injector and the tank ullage. Having cooled the ullage, the vaporized secondary flow exits through the top of the injector and leaves the tank.

The TVS-augmented injector affects tank-filling in two ways: (1) the main flow is subcooled, so that more heat is required to vaporize the incoming liquid, and droplet heat transfer with the ullage is improved, and (2) the large surface area at the top of the injector provides an additional heat sink to remove heat from the tank ullage. Even if the primary flow stalls because tank pressure rises too high, the secondary flow will continue to remove heat from the ullage, so that eventually the tank pressure will fall, and the filling process can resume.

Fig. 5 shows the modifications to the fluid flow paths in and out of CRYOTE required for the TVS-Augmented NVF tests. Just after the flow's pressure and temperature are measured at AI50 and TC50, the secondary flow branches off. The secondary flow's pressure is significantly reduced by the Joule-Thomson (JT) orifice. This isenthalpic pressure drop changes the secondary flow to be two-phase flow at a lower temperature. An additional vent line is routed through the tank lid to carry out the vaporized secondary flow to a near-vacuum boundary.

Table 1 outlines significant events in NVF Test 20180403 and Test 20180404, conducted on April 3 and 4, 2018 respectively. The main difference between the two tests was the point in time and duration for

when the TVS was engaged. In Test 20180403, the TVS was on for 1497 s, whereas for Test 20180404, the TVS was on for 635 s. The model results will be compared to this data in Section 4.3.

3. Modeling approach

Numerical modeling of filling a tank at ambient temperature with liquid cryogen is highly complex. The physical processes are complex because the flow is two-phase, and the process involves both boiling and condensation with heat transfer between solid and fluid. The objectives of a numerical model of filling a cryogenic tank are to predict the chilldown and filling time and to estimate the amount of propellant consumption to chill down a tank. A computational model of the chilldown and propellant loading of the Space Shuttle External Tank containing liquid oxygen and hydrogen at Launch Complex 39B at Kennedy Space Center was developed using GFSSP [5]. Numerical modeling of the "charge-hold-vent" method of filling a cryogenic tank in space, described in Reference 1, was also performed using GFSSP [6].

3.1. Introduction to GFSSP

GFSSP is a general-purpose computer program for analyzing fluid flow and heat transfer in a complex network of fluid and solid systems. It employs a pressure based, finite volume algorithm that solves the mass and energy conservation equations at the nodes and the momentum
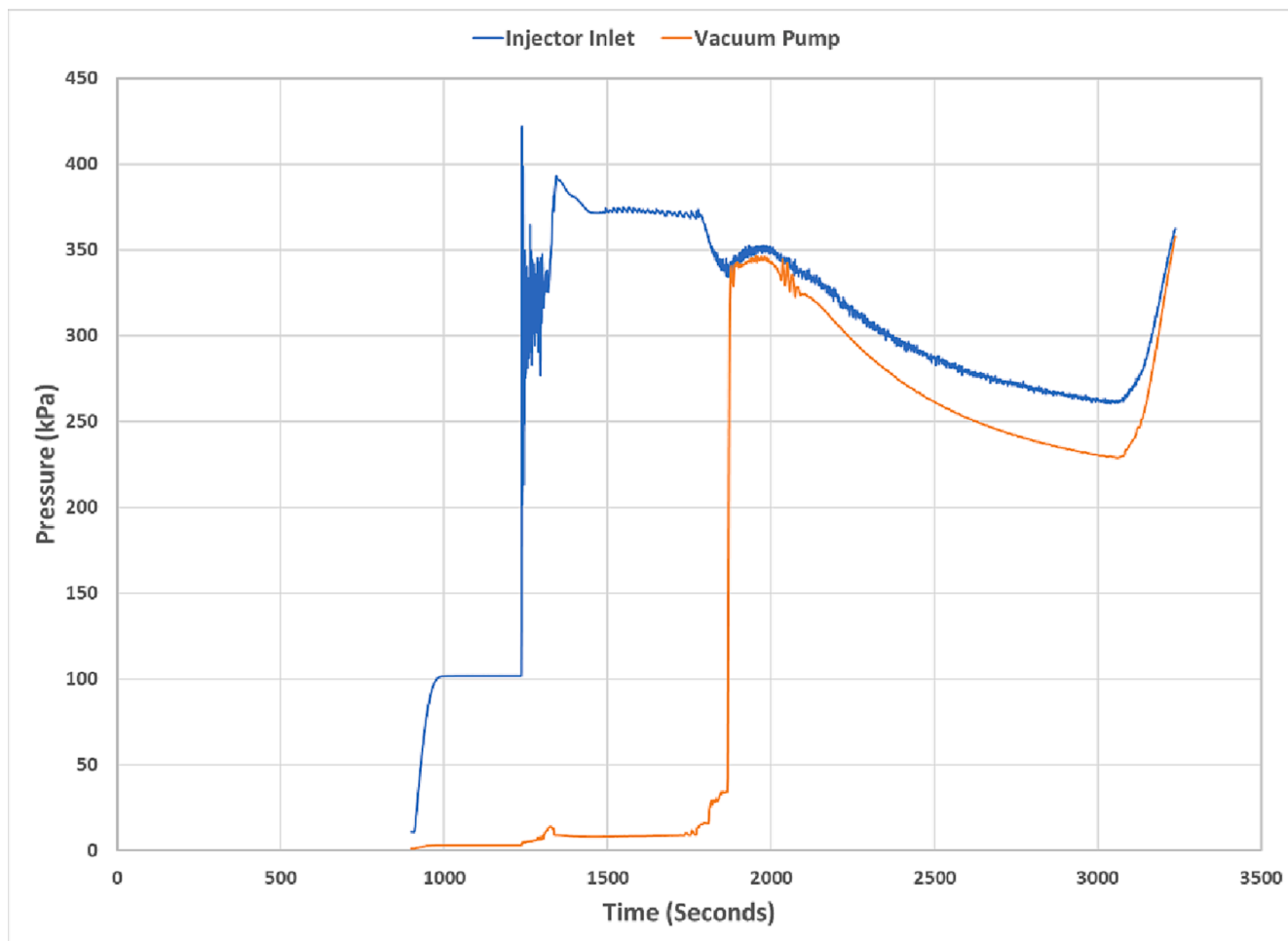
Fig. 10. Pressures at inlet of TVS Injector (Blue) and Vacuum Pump (Orange). (For interpretation of the references to colour in this figure legend, the reader is referred to the web version of this article.)

conservation equation at branches connecting the nodes. The energy conservation equations for solid are solved at solid nodes that are connected with fluid nodes to allow conjugate heat transfer. Thermodynamic properties are calculated for propellants using the computer program GASP [9], which is integrated with GFSSP. The fluid resistance library includes pipes, orifices, and common fittings and valves. GFSSP has three major parts. The first part is the graphical user interface MIG (Modeling Interface for GFSSP). MIG allows users to create a flow circuit by a "point and click" paradigm. It creates the GFSSP input file after the completion of the model building process. It can also create a customized GFSSP executable by compiling and linking User Subroutines with the solver module of the code. The user can run GFSSP from MIG and post process the results in the same environment. The second major part of the program is the Solver and Property Module. This is the heart of the program, which reads the input data file and generates the required conservation equations for fluid and solid nodes and branches with the help of thermodynamic property programs. It also interfaces with User Subroutines to receive any specific inputs from users. Finally, it creates output files for MIG to read and display results. The User Subroutine is the third major part of the program. This consists of several blank subroutines that are called by the Solver Module. These subroutines allow the users to incorporate any new physical model, resistance option, fluid, etc. in the model.

3.2. Finite volume formulation

In the Finite Volume Formulation [7], a thermo-fluid system is

discretized into a finite number of nodes and branches to represent a flow network consisting of different flow components such as pipes, valves, and orifices. Many thermo-fluid systems, including the chilling of a cryogenic tank, need to model solid to fluid (conjugate) heat transfer. In that situation, the solid wall in contact with the fluid is also discretized into solid nodes.

The mass and energy conservation equations are solved at the fluid nodes. The momentum conservation equations are solved at the flow branches. The energy conservation equations for the solid are solved at the solid nodes. The thermodynamic and thermo-physical properties required to construct the conservation equations are calculated using a thermodynamic property program that provides the properties of a real fluid for all possible states e,g. liquid, vapor, saturation, or super-critical.

3.2.1. Governing equations

The GFSSP Users' Manual [4] provides a detailed description of all governing equations. This section provides a brief description of the conservation equations and other empirical correlations used in the development of the tank chill and fill model. Fig. 6 displays a schematic showing adjacent nodes, their connecting branches, and the indexing system.

GFSSP calculates pressure from the mass conservation equation. The mass conservation equation for node i can be expressed as:

$$\frac{m_{\tau+\Delta\tau} - m_\tau}{\Delta\tau} = -\sum_{j=1}^{j=n} \dot{m}_{ij} \qquad (1)$$
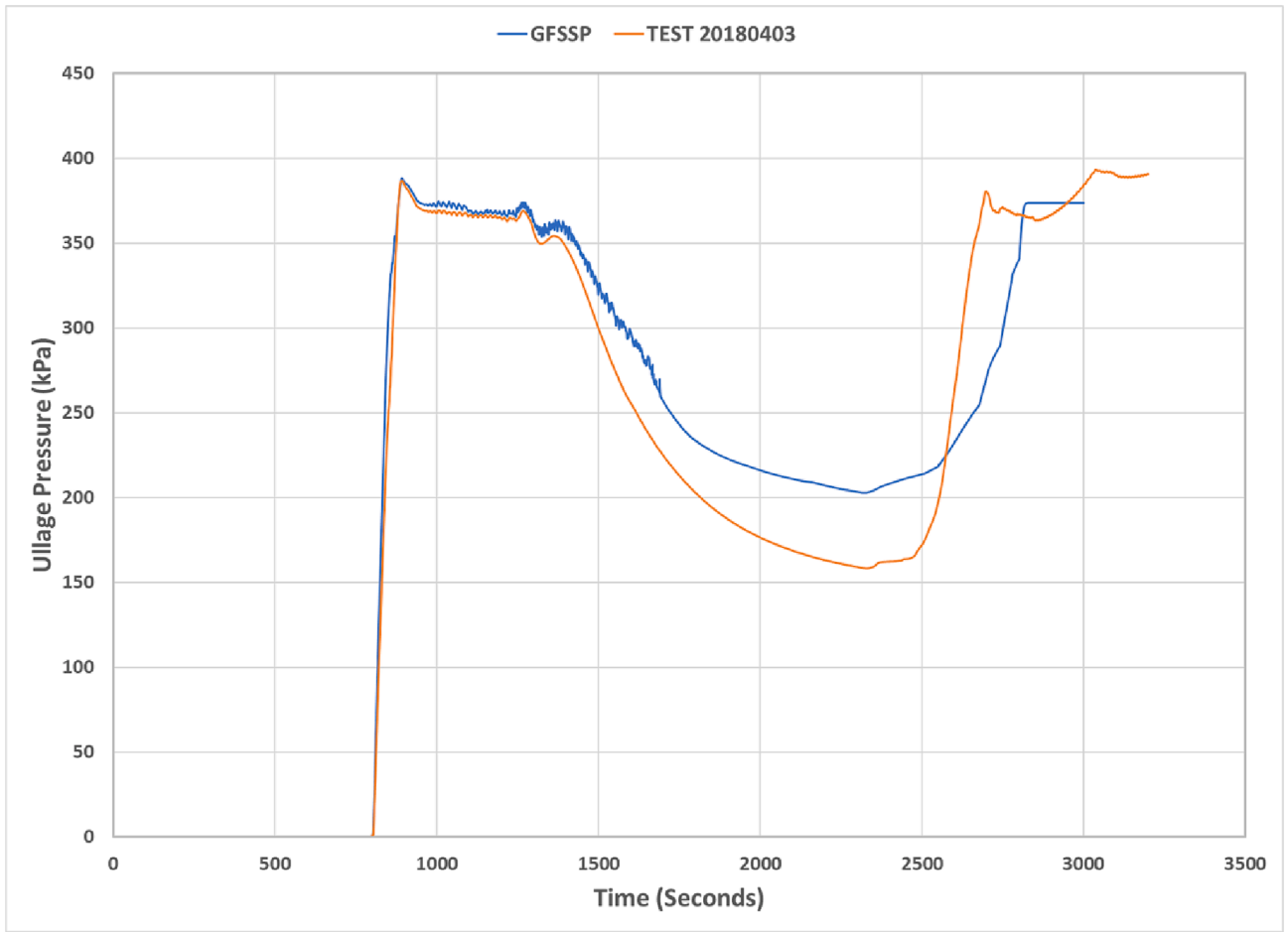
Fig. 11. Comparison of measured and predicted Tank Pressure for Test 20180403.

Fig. 7 shows the schematic of a Branch. It may be noted that the mass flow is driven by pressures which are located at the nodes (*i* and *j*). The gravity acts vertically downward. The angle between flowrate and gravity vector is θ.

GFSSP calculates flow rate from the momentum conservation equation which can be written as:

$$(p_i - p_j)A_{ij} + \frac{\rho g V \text{Cos}\theta}{g_c} - K_f \dot{m}_{ij} \left| \dot{m}_{ij} \right| A_{ij} = 0 \tag{2}$$

The first term in Equation (2) is the pressure force applied on the fluid. The second term represents the gravitational force. It may be noted that at θ = 180° the fluid is flowing against gravity; at θ = 90° the fluid is flowing horizontally, and gravity has no effect on the flow. The third term represents the frictional effect. Friction was modeled as a product of K_f and the square of the flow rate and area. K_f is a function of the fluid density in the branch and the nature of the flow passage being modeled by the branch. The calculation of K_f for different types of flow passages is described in reference [4].

The energy conservation equation is expressed in terms of enthalpy which is solved at the nodes:

$$\frac{m\left(h - \frac{p}{\rho J}\right)_{\tau + \Delta\tau} - m\left(h - \frac{p}{\rho J}\right)_{\tau}}{\Delta\tau} = \sum_{j=1}^{j=n}\left\{MAX\left[-\dot{m}_{ij}, 0\right]h_j - MAX\left[\dot{m}_{ij}, 0\right]h_i\right\} + Q_i \tag{3}$$

The left-hand side of Eq. (3) represents the rate of change of internal energy. The first term in the right-hand side represents the net influx of energy due to advection. The MAX operator used in Eq. (3) is known as

an upwind differencing scheme and has been extensively employed in the numerical solution of Navier-Stokes equations in convective heat transfer and fluid flow applications [8]. When the flow direction is not known beforehand, this operator allows the transport of energy only from its upstream neighbor. In other words, the upstream neighbor influences its downstream neighbor but not vice versa. Q_i represents any external heat source.

The resident mass at the node is calculated from the equation of state which can be expressed as:

$$m = \frac{pV}{zRT} \tag{4}$$

z is the compressibility factor of the fluid which is derived from thermodynamic properties. All thermodynamic and thermo-physical properties are calculated by the GASP computer code [9] from the calculated pressure and enthalpy at the nodes. It may be noted that Eq. (4) is valid for liquid, vapor, and liquid–vapor mixture.

For a two-phase saturated mixture, z is computed from the following relation.

$$z = \frac{p}{\rho_{mix}RT} \tag{5}$$

where $\rho_{mix} = \frac{\rho_l \rho_g}{x \rho_l - (1 - x)\rho_g}$ $\tag{6}$

and, $x = \frac{h - h_f}{h_g - h_f}$ $\tag{7}$

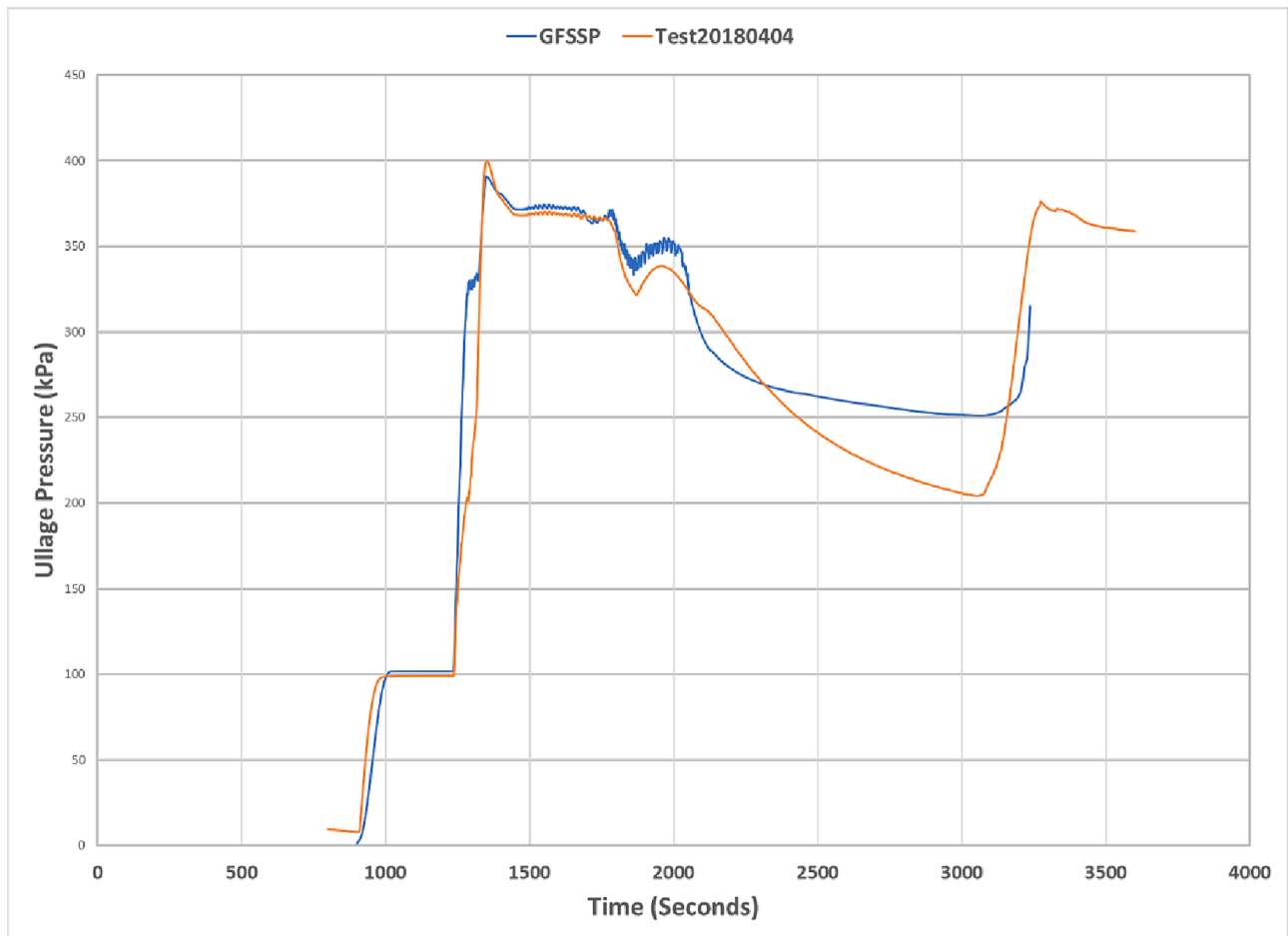The energy conservation equation for the solid is solved at the solid

Fig. 12. Comparison of measured and predicted Tank Pressure for Test 20180404.

node and is expressed as:

$$\frac{\partial}{\partial \tau}\left(mC_p T_s^i\right) = \sum_{j_f=1}^{n_{sf}} \dot{q}_{sf} + S_i \tag{8}$$

The left-hand side of the equation represents the rate of change of energy. The first term in the right-hand side represents convective heat transfer between fluid and solid node and is expressed in Eq. (9):

$$\dot{q}_{sf} = H_{ij_f} A_{ij_f}\left(T_f^{j_f} - T_s^i\right) \tag{9}$$

The parameter S_i represents any external heat source.

3.2.2. Numerical solution

GFSSP numerically solves the governing equations to compute pressure, enthalpy, flowrate and other fluid properties in a given flow circuit. The mathematical closure is described in Table 2 where each variable and the designated governing equation to solve that variable are listed. It may be noted that the pressure is calculated from the mass conservation equation although pressure does not explicitly appear in Eq. (1). This is, however, possible in the iterative scheme where pressures are corrected to reduce the residual error in the mass conservation equation.

3.3. Pool boiling model

The chilldown of a propellant tank is primarily governed by boiling of liquid propellant at the tank wall. Initially, the difference between the solid wall surface temperature and saturation temperature (wall superheat) is typically several hundred degrees. Therefore, the boiling starts

in the Film Boiling regime and continues until it reaches the Leidenfrost (Minimum Film Boiling, MFB) point. After reaching the Leidenfrost point, it switches to Transition Boiling and continues to Critical Heat Flux. Nucleate Boiling starts after reaching Critical Heat Flux and, finally, heat transfer is controlled by natural convection beyond the Onset of Nucleate Boiling (ONB) point.

3.3.1. Film boiling correlation

The heat transfer coefficient during film boiling was evaluated using the correlation of Wang et al [10], which can be expressed as:

$$H_{FB} = C(R(\frac{\lambda'}{c_{p,v}\Delta T}))^m(\frac{k_v}{L_x}) \tag{10}$$

$$R = (\frac{L_x^3 \rho_v (\rho_f - \rho_v)g}{\mu^2})(\frac{c_{p,v}\mu}{k_v}) \tag{11}$$

For a spherical tank,
$$C = 0.15; \; m = 1/3; \; L_x = Tank\,Diameter$$

$$\lambda' = h_{fg} + 0.5c_{p,v}\Delta T \tag{12}$$

3.3.2. Leidenfrost point

Leidenfrost point was calculated using the Baumeister and Simon [11] correlation which can be expressed as:

$$\Delta T_{LFP} = \frac{27}{32}T_C(1 - e^{-0.52 \times 10^4(\frac{\rho_S}{M_S})^{1/3}\frac{1}{\sigma}}) - T_{sat} \tag{13}$$

3.3.3. Critical heat flux

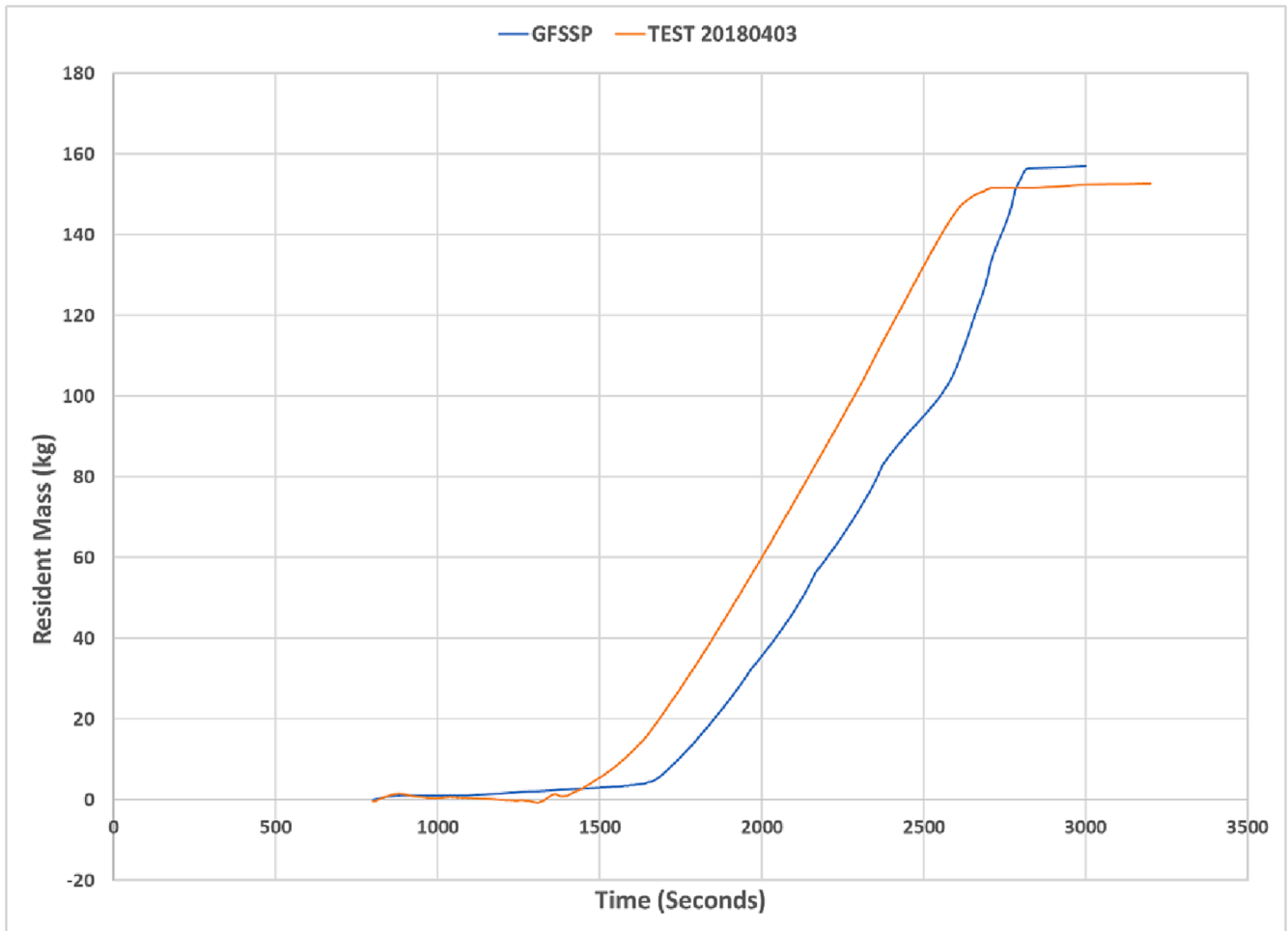The critical heat flux was calculated using Lienhard and Dhir's [12]

Fig. 13. Comparison of measured and predicted Resident Mass for Test 20180403.

correlation which is expressed as:

$$q''_{CHF} = f(l') \frac{\pi}{24} \rho_v^{\frac{1}{2}} h_{fg} \left(\sigma g \left(\rho_f - \rho_v \right) \right)^{\frac{1}{4}} \tag{14}$$

For a large spherical tank, $f((l')) = 0.84$

3.3.4. Transition boiling

The heat transfer coefficient during transition boiling is evaluated by logarithmic interpolation between the Leidenfrost and Critical Heat Flux points.

$$H_{TB} = e^{\left(\frac{\ln(H_{LFP}) - \ln(H_{CHF})}{\ln(\Delta T_{LFP}) - \ln(\Delta T_{CHF})} (\ln(\Delta T) - \ln(\Delta T_{CHF})) + \ln(H_{CHF}) \right)} \tag{15}$$

where

$$H_{CHF} = A_{CHF} \Delta T_{CHF}^{2.33} \tag{16}$$

$$A_{CHF} = (8.7 \times 10^{-4} (\frac{B}{h_{fg}\rho_v\nu_f})^{0.7} (\frac{PB}{\sigma})^{0.7} (\frac{k_f}{B}))^{3.33} \tag{17}$$

3.3.5. Nucleate boiling

The heat transfer coefficient is calculated from Borishansky et al [13] correlation which can be expressed as:

$$H_{NB} = A_{NB} \Delta T^{2.33} \tag{18}$$

$$A_{NB} = (8.7 \times 10^{-4} (\frac{B}{h_{fg}\rho_v\nu_f})^{0.7} (\frac{PB}{\sigma})^{0.7} (\frac{k_f}{B}))^{3.33} \tag{19}$$

3.3.6. Natural convection

The heat transfer coefficient during natural convection was calculated using the correlation of Shirai et al [14]:

$$H_{NC} = 0.16 \frac{k_f}{L_c} (Pr_f Gr_f)^{1/3} \tag{20}$$

3.3.7. Onset of Nucleate Boiling (ONB)

ΔT_{ONB} is calculated by setting H_{NB} equal to H_{NC} and solving for ΔT:

$$\Delta T_{ONB} = (\frac{A_{NC}}{A_{NB}})^{0.5} \tag{21}$$

$$A_{NC} = \frac{H_{NC}}{\Delta T^{\frac{1}{3}}} \tag{22}$$

Finally, once all the terms have been defined according to the equations above, the correct heat transfer coefficient is determined depending on the wall superheat using the following logic:

If $0 < \Delta T \leq \Delta T_{ONB}$

Use H_{NC}

Else if $\Delta T_{ONB} < \Delta T \leq \Delta T_{CHF}$

Use H_{NB}

Else if $\Delta T_{CHF} < \Delta T \leq \Delta T_{LFP}$

Use H_{TB}
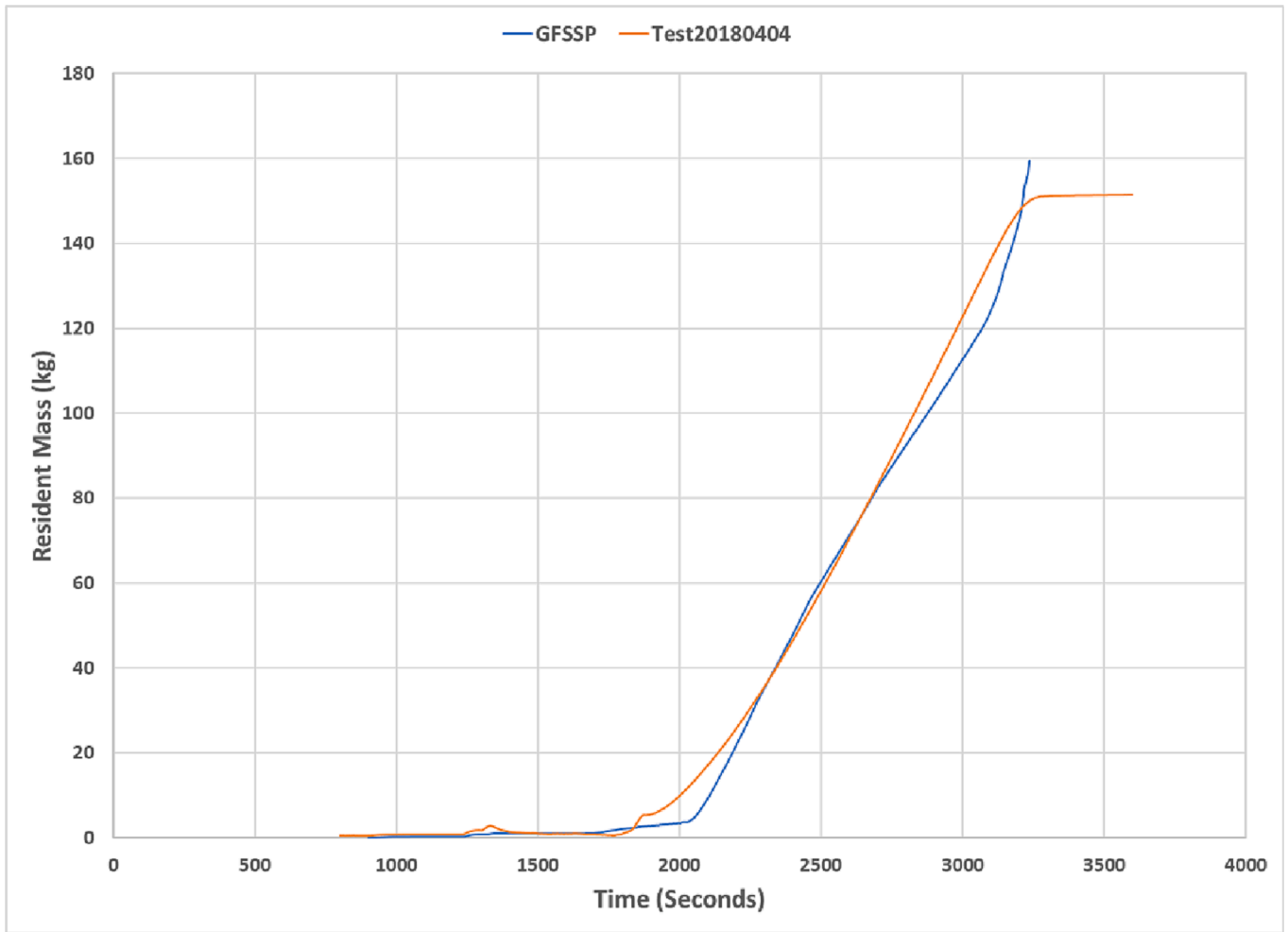
Else if $\Delta T_{LFP} \leq \Delta T$

Use H_{FB}

Fig. 14. Comparison of measured and predicted Resident Mass for Test 20180404.

3.4. Condensation model

3.4.1. Condensation on a droplet

Some of the vapor in the tank ullage condenses during the process of filling the tank by spraying liquid propellant in the tank. Condensation of vapor occurs when vapor comes in contact with subcooled liquid spray. Condensation reduces the tank pressure and therefore must be accounted for in the numerical model to predict the pressure and the resident liquid mass in the tank. A simple condensation model has been developed for the present analysis.

It is assumed that the liquid spray in the tank remain in the form of droplets of constant effective diameter. The saturated vapor in contact with the liquid droplet rejects the latent heat of vaporization to condense. At any time, the total number of droplets in the tank can be found from

$$N_i = \frac{\dot{m}_i \Delta \tau_{res}}{\frac{\pi d^3}{6}\rho_L} \tag{23}$$

where the residence time is found from

$$\Delta \tau res = \frac{\Delta H}{U_{inj}} \tag{24}$$

In this equation ΔH is a characteristic length scale. In this analysis it was assumed to be equal to the radius of tank. U_{inj} is the velocity at the injector determined from the mass flowrate, injector area and upstream density.

The heat transfer from vapor to liquid can be calculated from the following expressions:

$$\dot{q} = HA(T_{sat} - T_L) \tag{25}$$

$$A = N_i \pi d^2 \tag{26}$$

$$H = \frac{k_L}{d}Nu_{D,in} \tag{27}$$

According to Kronig and Brink [15] $Nu_{D,in} = 17.9$. Spray droplets are known to have a wide size distribution and typically cover a size spectrum in the 10 to 1000 μm range, with mean droplet diameters of a few hundred μm [17,18,19]. CFD simulations also model sprays by using a constant effective spray droplet diameter [20]. Accordingly, the average droplet diameter in this study is assumed to be 1.5 mm.

The condensation rate per unit volume is expressed as

$$\dot{m}'' = \frac{\dot{q}}{\lambda V} \tag{28}$$

3.4.2. Condensation at injector ullage interface

Fig. 8 shows the schematic of the condensation model at Injector-Ullage interface. The injector is cooled by the internal flow of cold vapor produced by the J-T valve. Ullage vapor is condensed at this cold surface. Condensation occurs on a thin condensate liquid film where the liquid film-ullage interface remains at saturation temperature corresponding to the ullage pressure near the solid surface. The condensation rate is calculated from an energy balance applied to the liquid-ullage interface [21]. The governing equations are:
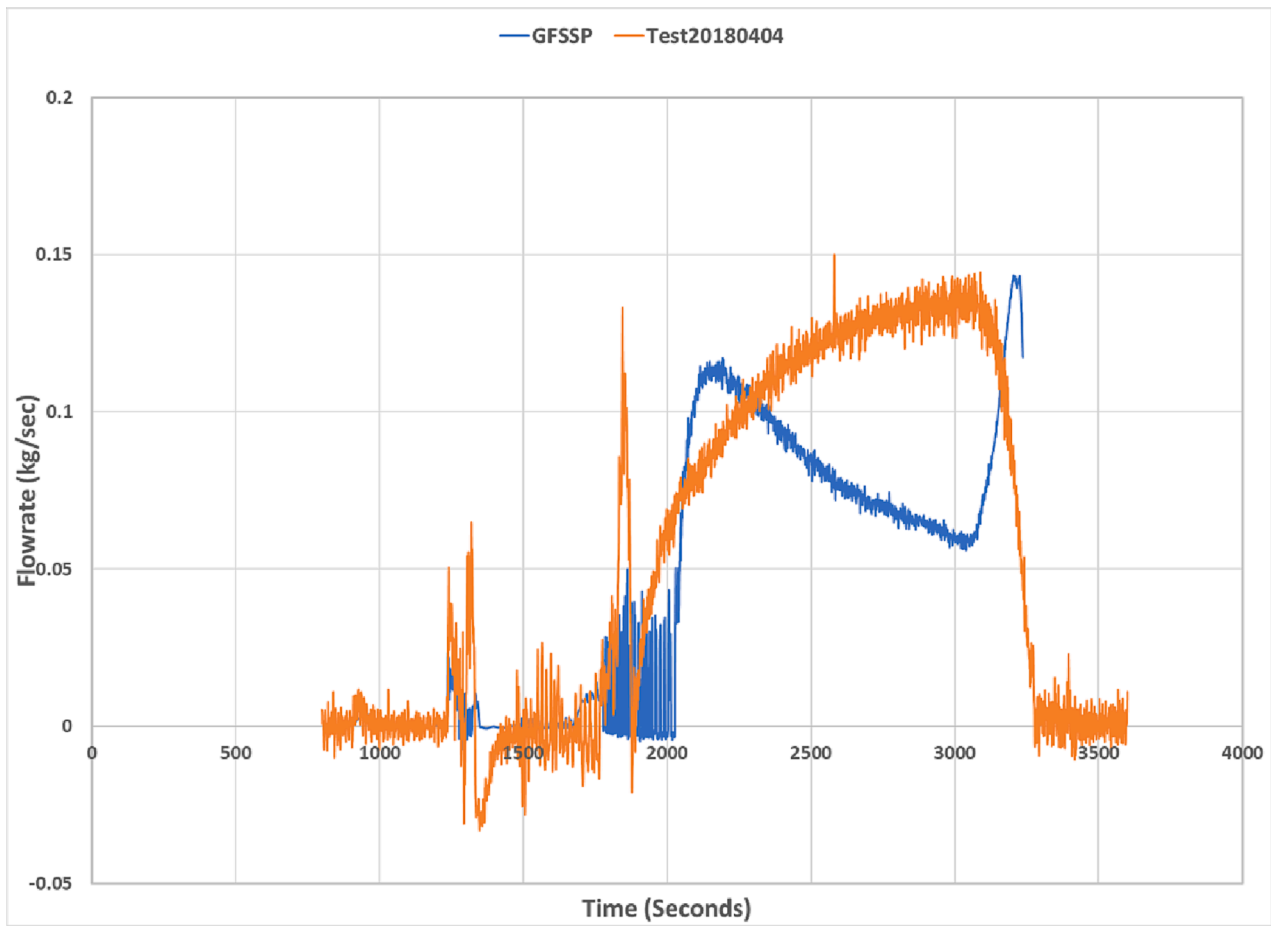
Fig. 15. Comparison of measured and predicted Flowrate for Test 20180404.

Heat transfer from Ullage to condensate layer

$$\dot{Q}_{US} = H_{US}A_{eff}(T_U - T_S) \tag{29}$$

Heat transfer through the condensate layer to wall

$$\dot{Q}_{SW} = H_{SW}A_{eff}(T_S - T_W) \tag{30}$$

Energy Balance across the liquid-ullage interface leads to

$$\dot{Q}_{SW} - \dot{Q}_{US} = \dot{m}_{cond}h_{fg} \tag{31}$$

Heat transfer between ullage and the condensate film surface is assumed to be by free convection, and is modeled as laminar film condensation around an impermeable horizontal cylinder imbedded in a porous structure [22], thereby

$$Nu_{US} = \frac{H_{US}D^{'}}{k_g} = 0.565\,Ra_D^{1/2} \tag{32}$$

$$Ra_D = \frac{Kg\beta|T_U - T_S|D^{'}}{\propto_g v_g} \tag{33}$$

$$D^{'} = D_{tube} + \delta_L \tag{34}$$

$$K = \frac{\epsilon\delta_L^2}{32} \tag{35}$$

Note that for simplicity and in view of the uncertainties with respect various aspects of the geometric and flow conditions the effect of mass transfer on convective heat transfer is not included in the above formulations.

The rate of heat transfer from the liquid-ullage interface through the

condensate liquid film to the wall is estimated by considering conduction through the porous structure that is filled with a condensate liquid layer, thereby

$$H_{SW} = \frac{\varepsilon k_L + (1 - \varepsilon)k_W}{\delta_L} \tag{36}$$

$$\varepsilon = \frac{V_f}{V} \tag{37}$$

$$D_H = \frac{4V_f}{A} = \frac{4\varepsilon V}{A} \tag{38}$$

$$\delta_L = \alpha D_H \tag{39}$$

where the liquid condensate film thickness has been assumed to be proportional to the effective hydraulic diameter D_H associated with flow through the porous layer with α being an empirically adjusted parameter. In Eq. (36) k_L and k_W represent the thermal conductivities of saturated liquid and the solid porous structure, respectively.

Table 3 depicts the geometrical parameters of the TVS augmented injector shown in Fig. 4 extracted from CAD Drawings. The porosity and effective hydraulic diameter of the porous structure were estimated to be 0.76 and 8.46 mm (0.1328 inch), respectively. In the present model α was set to 0.175.

3.4.3. Condensation at the liquid pool-vapor interface

The interface of liquid and vapor remains saturated with respect to the local pressure. At the liquid–vapor interface, there is a possibility of either evaporation or condensation depending upon the condition of ullage vapor and liquid. The phase change occurs as a result of
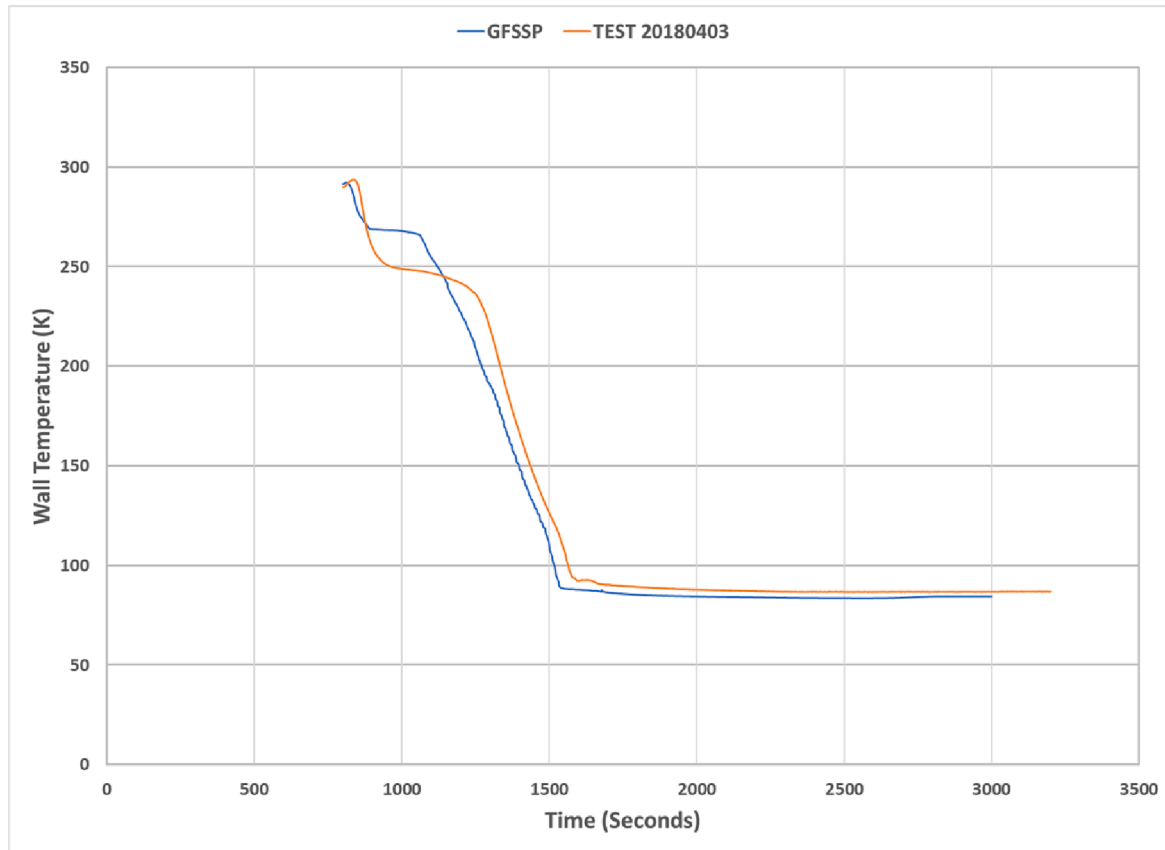
Fig. 16. Comparison of measured and predicted Wall Temperature at 16% Fill Level for Test 20180403.

imbalance between heat transfer rates on the vapor and liquid sides of the saturated interface. If the heat transfer from the ullage to the interphase (Q_{UI}) is larger than the heat transfer from the interphase to liquid (Q_{IL}), evaporation of liquid occurs at the interface. On the other hand, if the heat transfer from the interphase to liquid (Q_{IL}) is larger than the heat transfer from the ullage to the interphase (Q_{UI}), condensation of vapor occurs at the interface.

The governing equations are:

Heat Transfer from ullage to the interphase

$$\dot{Q}_{UI} = H_{UI}A(T_U - T_I) \tag{40}$$

Heat Transfer from the interphase to liquid

$$\dot{Q}_{IL} = H_{IL}A(T_I - T_L) \tag{41}$$

Condensation rate from energy balance

$$\dot{m} = \frac{\dot{Q}_{IL} - \dot{Q}_{UI}}{h_{fg}} \tag{42}$$

The ullage-interphase heat transfer is idealized as free convection between a horizontal surface underneath a large gas space, thereby [21,23,24]

$$H_{UI} = K_H C \frac{k_f}{L_s} Ra^n = H_{IL} \tag{43}$$

where Ra represents the Rayleigh number in which the length scale is L_s, defined as

$$L_s = A/P \tag{44}$$

where A and P represent the pool surface area and perimeter, respectively. In Eq. (43), we have $K_H = 0.5$, $C = 0.27$, and $n = 0.25$.

h_{UI} is based on vapor properties and h_{IL} is based on liquid properties.

3.5. Tracking of liquid-vapor interface

To calculate condensation at the liquid vapor interphase, it is necessary to locate the interface node where the liquid surface resides as the tank fills from the bottom. The volume and surface area of the spherical sector are expressed in Eqs. (45) and (46)

$$V = \frac{\pi}{3}v^2(3R - v) \tag{45}$$

$$a = \sqrt{v(2R - v)} \tag{46}$$

Interface tracking is performed using the following steps:

Estimate the mass of liquid in the tank
Estimate the volume of the liquid in the tank
Estimate the liquid height, v, by solving Eq. (45) by the Newton-Raphson method
Interface node is determined by interpolation from the array of heights of all tank nodes

3.6. Estimation of pressure work on the ullage due to rising liquid surface

As the liquid level rises, vapor in the ullage is compressed. The pressure work is applied in the energy equation in the interface node. The pressure work is computed as:

$$P_W = \frac{P_{ullage}\frac{dV_{fill}}{d\tau}}{J} \tag{47}$$

4. Modeling of no vent fill test with TVS augmented injector

A GFSSP model of NVF Test with TVS augmented injector is described in this section. This model starts from the inlet of the TVS
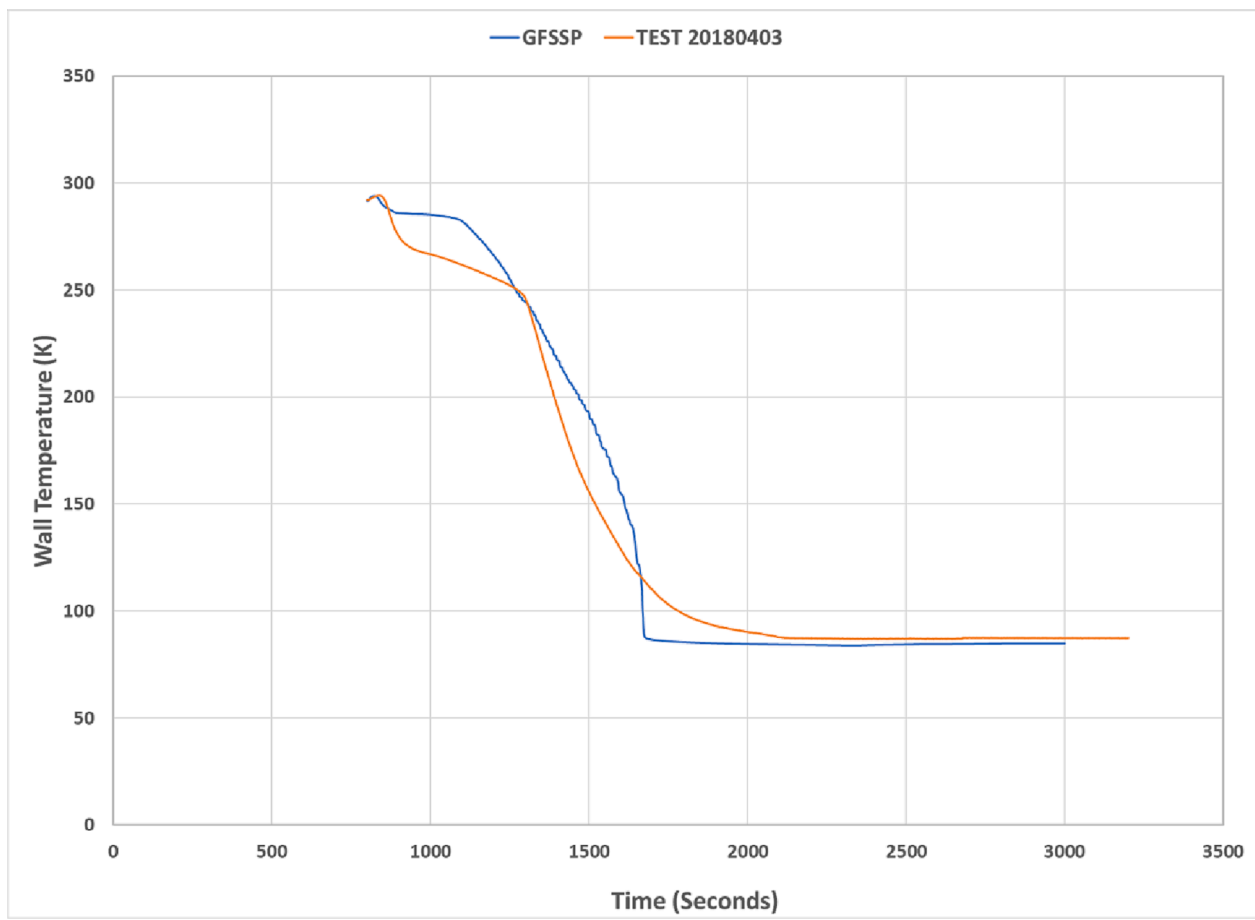
Fig. 17. Comparison of measured and predicted Wall Temperature at 48% Fill Level for Test 20180403.

augmented injector and includes J-T valve and the line leading to the vacuum pump. The vent line of the tank is included but the vent orifice is shut during the entire simulation. The transfer line from the VATA supply tank is not included.

4.1. GFSSP model of NVF experiment

The GFSSP model of NVF experiment is shown in Fig. 9. The model starts from the inlet to the injector (Node 2). The fluid is distributed to two parallel paths. A smaller portion of the flow goes through a J-T valve (Branch 5727) and exits through a vacuum pump represented by Node 29. In the J-T valve, the liquid is expanded to go through a change of phase and becomes a mixture of cold liquid and vapor. This cold mixture cools the Solid Node 30 which represents the injector surface (Fig. 4) in contact with the ullage. The larger portion of the flow goes through the injector represented by Node 32 and 9 restriction branches (321, 327, 328, 329, 3210, 3211, 3212, 3213, 3214). Each branch has identical resistance and therefore the injector provides uniform flow to 9 Tank Nodes (1, 7, 8, 9, 10, 11, 12, 13, 14). Note that the top tank node 15 does not receive any spray. However, it is cooled by the injector surface (Node 30).

4.2. Initial & boundary condition

Initially the CRYOTE Tank for NVF Test was at a vacuum pressure (1.14 kPa, 0.166 psi) and near room temperature (15.2 °C, 59.4 °F) because the vacuum pump was running before the opening of the inlet valve. The boundary pressures at inlet to the TVS augmented injector and at the inlet of vacuum pump are shown in Fig. 10. At Node 3 (upstream of the injector), the specific enthalpy was estimated from

measured pressure and temperature and assigned. For superheated vapor and subcooled liquid states, the specific enthalpy was calculated from measured pressure and temperature. However, for saturated conditions, enthalpy is a function of pressure and quality. From the measured data, the saturated states were identified (when temperature at Node 3 remains constant at saturation temperature) and quality has been assumed to vary linearly from 1.0 to 0.0 during this period (about 140 s).

4.3. Results and discussion

Test 20180403 and 20180404 [2] were simulated. In what follows the predicted tank pressure, filling of the tank, and chill down of the wall and ullage are compared with the test data. The predicted flowrate to the tank and condensation heat transfer results are also presented.

4.3.1. Pressure

Comparison of measured and predicted tank pressure for both tests is provided in Figs. 11 and 12. Tank filling starts at vacuum pressure because the vacuum pump downstream of the TVS injector was running before the opening of the fill valve. After the opening of the fill valve, tank pressure rises rapidly and becomes steady at the supply pressure. Due to cooling of the TVS injector, condensation takes place at the ullage-injector interface and pressure starts falling, allowing the liquid propellant to enter the tank. As a result, pressure falls farther, and the tank fills at a faster rate. As the tank fills, pressure again starts rising until the tank is full.

4.3.2. Resident mass and flowrate

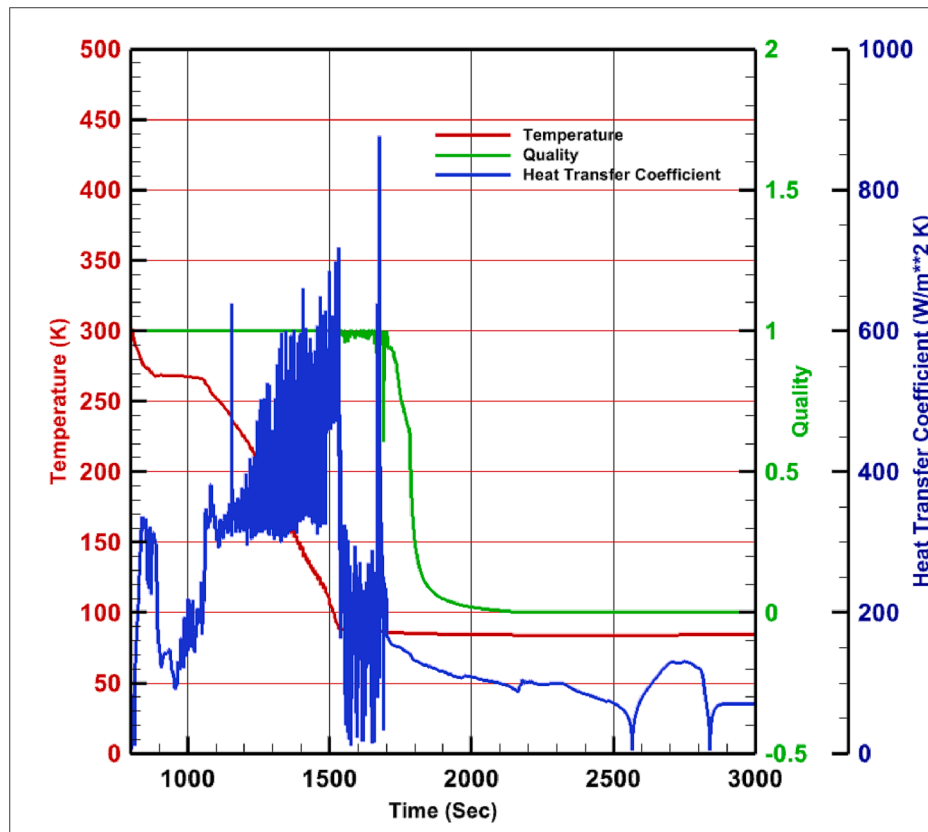Comparison of measured and predicted resident mass for both tests is

Fig. 18. Predicted Fluid Temperature, Quality and Heat Transfer Coefficient at 16% Fill Level for Test 20180403.

provided in Figs. 13 and 14. It takes about 2000 to 2400 s to fill the tank. Liquid does not start accumulating before 700 to 1000 s after the opening of the fill valve. During this time, the tank remains nearly stalled as can be seen in Figs. 13 and 14. After that the Tank fills at a nearly constant rate. The predicted and estimated flowrates for Test 20180404 are shown in Fig. 15. Note that flowrate has not been measured in the test and has been derived by taking a derivative of resident mass. There is reasonable agreement between the numerical predictions and test data considering the uncertainty of the experimental data and approximations of the condensation model.

4.3.3. Wall temperature

Comparison of measured and predicted Wall Temperature at 16% and 48% Fill Level for Test 20180403 is provided in Figs. 16 and 17, respectively. Note that the tank starts chilling down from the bottom. Generally, there is a reasonable agreement between the measured data and numerical predictions. The initial underprediction of cooling is possibly due to the assumption of one-dimensional flow in the tank. In reality, there may be a natural convection dominated recirculating flow in the tank; colder fluid at the central core tends to sink downward and the flow near the wall rises upward due to gravitational effect. A one-dimensional flow model does not account for such recirculating flow, which may be a cause of the discrepancy. The uncertainty in boiling heat transfer correlation could also contribute to the observed discrepancy.

4.3.4. Boiling

Predicted Fluid Temperature, Quality and Heat Transfer Coefficient at the 16% Fill Level for Test 20180403 are shown in Fig. 18. The fluid temperature history closely resembles the wall temperature history at the same fill level as shown in Fig. 16. At this fill level, fluid remains superheated for about 700 s. During this period, the heat transfer coefficient is calculated by the natural convection correlation given in Eq. (20). The variation in heat transfer coefficient is caused by rapid changes

in pressure and temperature. Two-phase flow occurs after $\tau = 1400$ s and continues for another 400 s until it becomes saturated liquid. During this period, pool boiling correlations as described in Section 3.3 were used to compute the heat transfer coefficient.

4.3.5. Condensation

Predicted condensation rates at the injector-ullage, spray-ullage and liquid–vapor interfaces for Test 20180404 are shown in Fig. 19. Condensation at the injector-ullage interface starts at 1650 s; condensation at the spray-ullage interface starts shortly afterwards. However, condensation at the liquid–vapor interface is insignificant compared to other two types of condensation. The effect of condensation at ullage-injector interface on tank pressure and inflow rate into the tank is shown in Fig. 20. It may be noted that a drop in pressure (Green) at 1690 s coincides with the rise of the condensation rate (Orange). The flowrate into the tank (Black) also starts during the same time. Therefore, condensation at the injector-ullage interface plays an important role in overcoming the stalling of the fill process.

The predicted temperature in the TVS line and injector and ullage temperature for Test 20180404 are shown in Fig. 21. The saturated temperature at the tank pressure is also shown in the figure. The ullage temperature first falls due to injection of cold fluid and then rises due to rapid tank pressurization. The temperature in the TVS line follow the inlet temperature and J-T effect. The injector temperature closely follows TVS line temperature. After 1650 s, the injector temperature falls below saturation temperature and condensation rate at injector-ullage surface rises as shown in Fig. 20.

The effect of condensation at the spray-ullage interface on tank pressure and inflow rate into the tank for Test 20180403 is shown in Fig. 22. Condensation at the spray-ullage interface also plays an important role in reducing the tank pressure and thereby allows the increase of flowrate into the tank. The reduction of tank pressure (Green) at 1780 sec coincides with a rise of the condensation rate
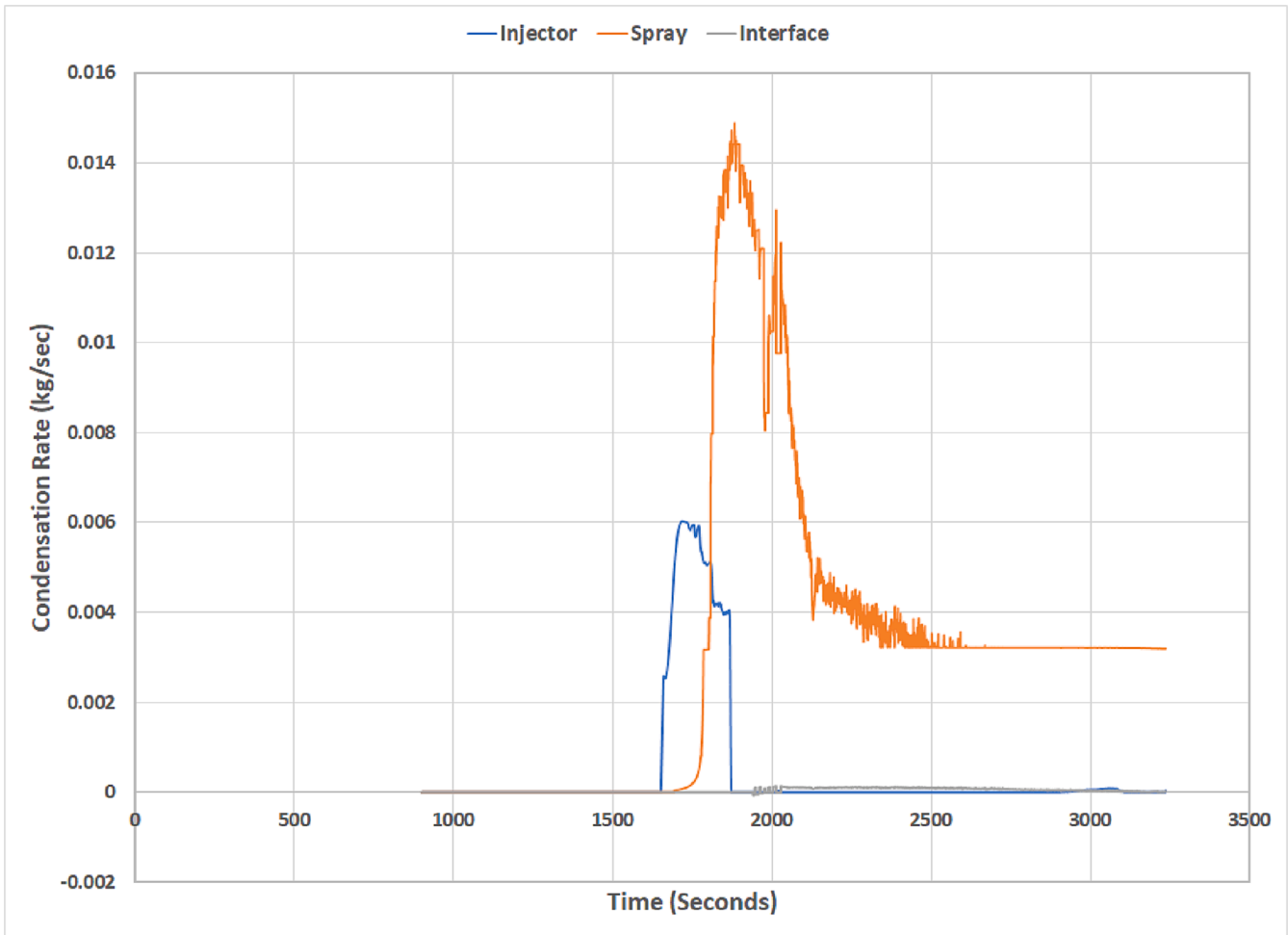
Fig. 19. Predicted Condensation Rates at Injector-Ullage (Blue), Spray-Ullage (Orange) and Liquid-Vapor Interfaces (Grey) for Test 20180404. (For interpretation of the references to colour in this figure legend, the reader is referred to the web version of this article.)
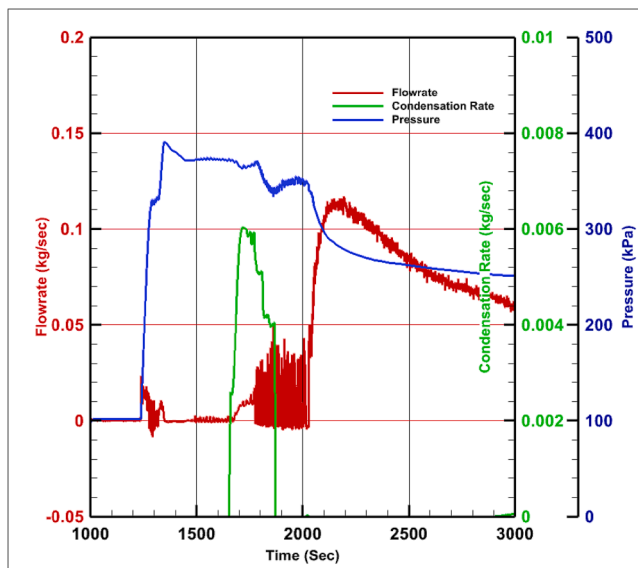

Fig. 20. Effect of Condensation at Ullage-Injector interface on Tank Pressure and Inflow Rate into the Tank for Test 20180404.

(Orange).

4.3.6. Tank filling

The growth of liquid volume and the location of the liquid–vapor interface as the tank fills for Test 20180403 are shown in Fig. 23. Liquid volume is calculated from the liquid mass which is calculated from total mass and vapor quality. From liquid volume, the height and radius of the interface were calculated from Eqs. (45) and (46). The interface node was determined by interpolation. The predicted liquid volume (VFILL) is shown in orange and the location of the interface node (IFILL) as the tank fills is shown in green.

It was also observed that during tank filling (Test 20180404) about 0.64 kg of nitrogen was vented out to ambient through TVS line. This amount is about 0.4% of total amount of liquid nitrogen filled in the tank. Therefore, the filling process with the TVS augmented injector is practically very close to no vent filling.

4.3.7. Effect of time step

All calculations presented in this paper were performed with a timestep of 0.01 s. In order to establish that the numerical solution is independent of time step, two additional simulations of Test 20180404 were performed with 0.002 and 0.05 s time step. The effect of timestep on predicted pressure is shown in Fig. 24. The green line represents the solution with a timestep of 0.01 s and the orange line represents the solution with a timestep of 0.05 s and blue line represents the solution with 0.002 s time step. It can be concluded that the numerical solution is practically independent of time step. There is also a proportional
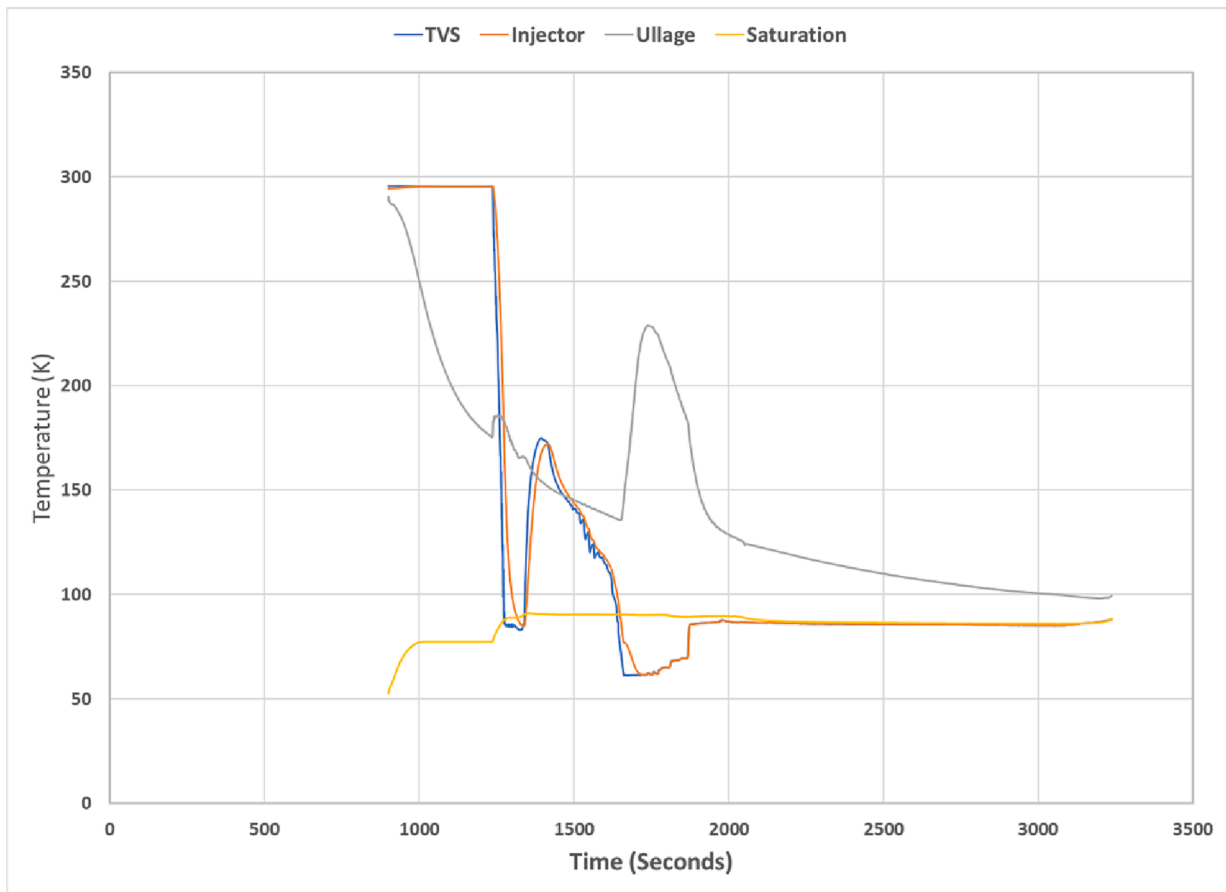
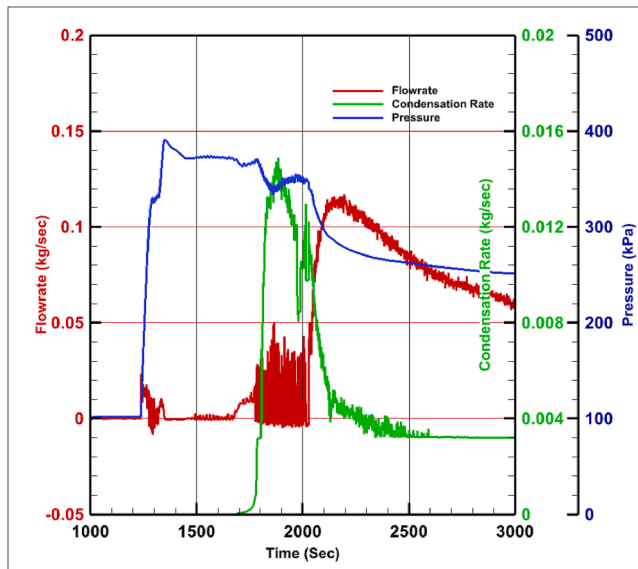**Fig. 21.** Predicted Temperatures at TVS (Fluid Node 28), Injector (solid Node 30), Ullage (Fluid Node 15) and Saturation.

Fig. 22. Effect of Condensation at Spray-Ullage interface on Tank Pressure and Inflow Rate into the Tank for Test 20180404.
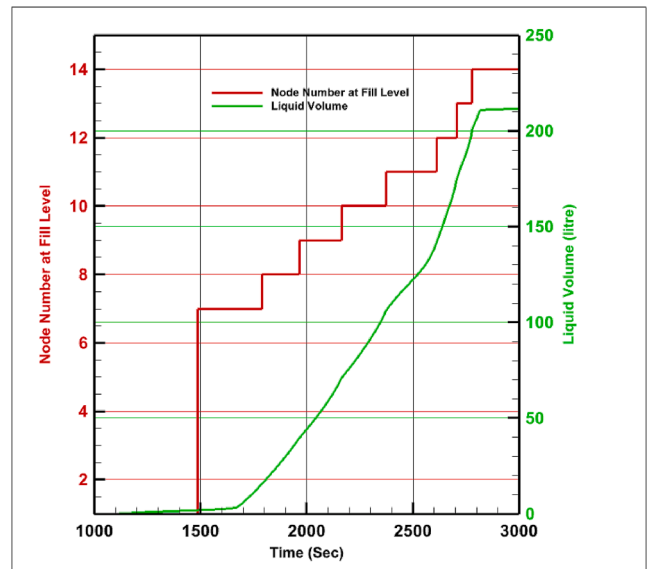

Fig. 23. Growth of Liquid Volume (Orange) and Location of Liquid Vapor Interface (Green) represented by Node Number (described in Fig. 10) as Tank fills for Test 20,180,403. (For interpretation of the references to colour in this figure legend, the reader is referred to the web version of this article.)

reduction in computational time when run with a larger time step and proportional increase in computational time with a smaller time step.

5. Conclusions

Numerical modeling of No Vent Fill of a Cryogenic Tank is complex

for several reasons. The flow is two-phase with both boiling and condensation taking place during the operation. During rapid chilling of the tank, different regimes of pool boiling occur: Film Boiling, Transition Boiling, Nucleate Boiling, and Natural Convection. The flow is stratified,
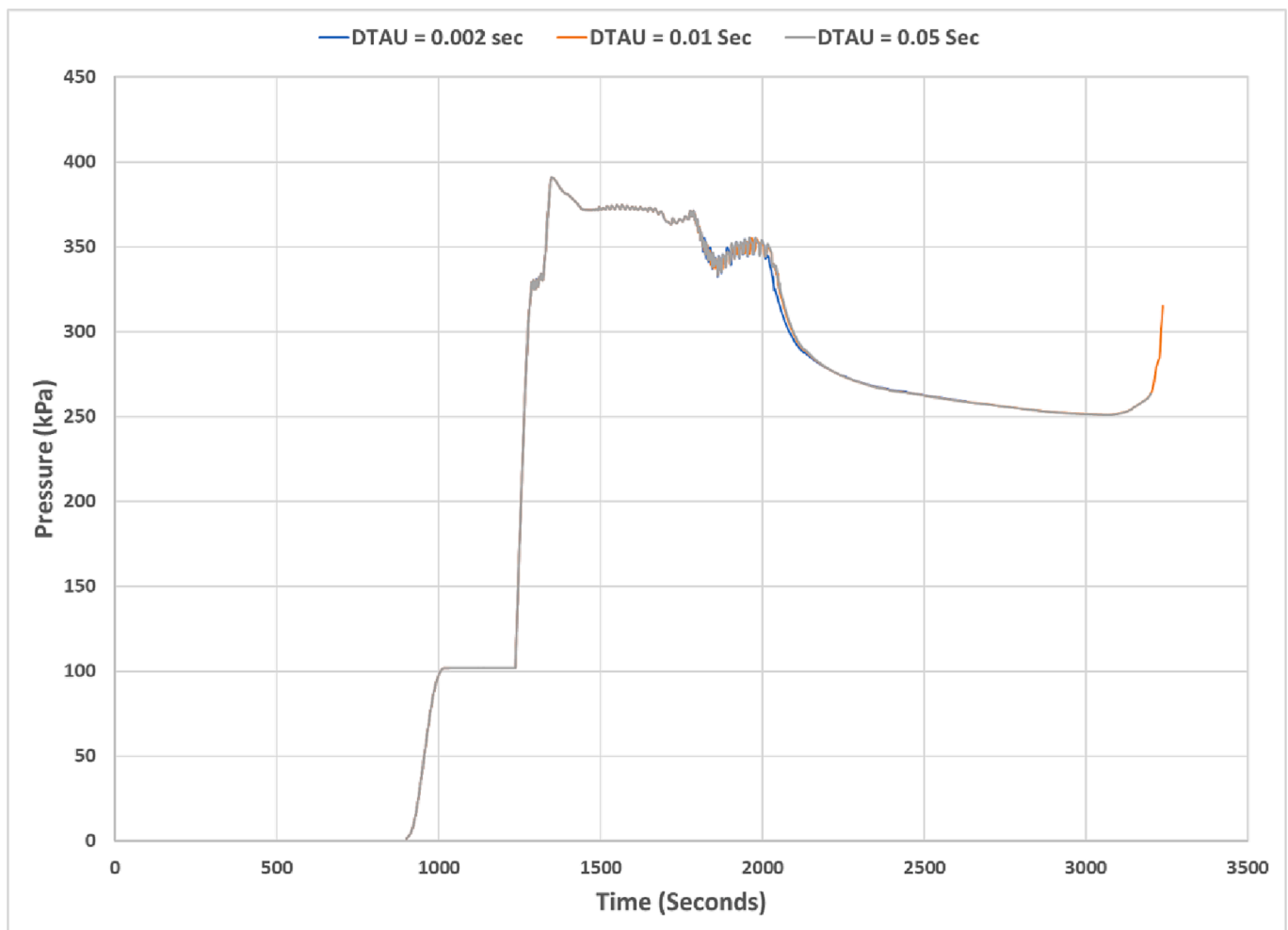
Fig. 24. Effect of Timestep on Tank Pressure for Test 20180404.

and the liquid–vapor interface is rising as the tank fills up. Condensation plays a critical role in tank filling. In the absence of condensation, the tank fails to fill and remains stalled.

In this paper, a system level network flow model was developed using GFSSP. Flow in the tank was assumed one-dimensional. The emphasis in the model is on the thermodynamics and heat transfer. The model includes all regimes of pool boiling and condensation at injector, spray, and liquid–vapor interfaces. Empirical models of condensation have been developed for the TVS augmented injector, around liquid droplets from the spray injector, and at the liquid–vapor interface. The model includes a tracking algorithm to locate the interface of the rising liquid in the tank. Pressure work on the ullage due to the rising liquid level is also considered. The numerical predictions of pressure and tank filling time compare with the measured data within 20% and 4% respectively. Numerical stability and convergence of the solution has been ensured by performing a timestep sensitivity study.

Declaration of Competing Interest

The authors declare that they have no known competing financial interests or personal relationships that could have appeared to influence the work reported in this paper.

Data availability

Data will be made available on request.

References

[1] Chato David, Sanabria Rafael. Review and test of chilldown methods for space-based cryogenic tanks, NASA Tech Memor 104458: AIAA-91-1843.

[2] Keefer K, Hartwig JW, Chato DJ. Development and validation of an analytical charge-vent-hold model for cryogenic tank chilldown. Int J Heat Mass Transf 2016; 101:175–89.

[3] Hartwig JW, Rhys N, Stevens J, Clark J, LeClair A, Majumdar A. Test data analysis of the CRYOTE-2 TVS augmented top spray injector liquid nitrogen transfer experiments. Int J Heat Mass Transf 2022;194:122986.

[4] Generalized Fluid System Simulation Program. Version 6.0, User Manual; March 2016. NASA/TP-2016-218218.

[5] LeClair Andre, Majumdar Alok. Computational model of the chilldown and propellant loading of the space shuttle external tank. In Paper No. AIAA 2010-6561, 46th AIAA/ASME/SAE/ASEE Joint Propulsion Conference & Exhibit, 25-28 July; 2010.

[6] Majumdar Alok. No vent tank fill and transfer line chilldown analysis by GFSSP. Presented in Thermal & Fluids Analysis Workshop (TFAWS 2013), Florida: Kennedy Space Center, July 29–August 2; 2013.

[7] Majumdar Alok. A finite volume procedure for thermofluid system analysis in a flow network. 50 Years of CFD in Engineering Sciences, A Commemorative Volume in Memory of D. Brian Spalding, Springer; 2020. p. 231–65.

[8] Patankar SV. Numerical heat transfer and fluid flow. Washington, D. C.: Hemisphere Publishing Corp; 1980.

[9] Hendricks RC, Baron AK, Peller IC. GASP – A computer code for calculating the thermodynamic and transport properties for ten fluids: parahydrogen, helium, neon, methane, nitrogen, carbon monoxide, oxygen, fluorine, argon, and carbon dioxide. NASA TN D-7808; February, 1975.

[10] Lei Wang, Jiaojiao Wang, Tian Yan, Shixuan Ye, Fushou Xie, Yanzhong Li. Film boiling heat transfer prediction of liquid nitrogen from different geometry heaters. Int J Multiphase Flow; August 2020.

[11] Baumeister K, Simon F. Leidenfrost temperature—its correlation for lipid metals, cryogens, hydrocarbons, and water. J Heat Transfer 1973;95(2):166–73.

[12] Lienhard J, Dhir V. Hydrodynamic prediction of peak pool-boiling heat fluxes from finite bodies. J Heat Transfer 1973;95(2):152–8.

[13] Borishansky VM, Bodrovich BI, Minchenko FP. "Heat transfer during nucleate boiling of water and ethyl alcohol", published in a volume of collection of articles. In: Kutateladze SS, editor. Aspects of Heat Transfer and Hydraulics of Two-Phase Mixtures. Moscow: Govt. Energy Publishing House; 1961. p. 75–93.

[14] Shirai Y, Tatsumoto H, Shiotsu M, Hata K, Kobayashi H, Naruo Y. Boiling heat transfer from a horizontal flat plate in a pool of liquid hydrogen. Cryogenics 2010: 410–6.

[15] Kronig R, Brink JC. On the theory of extraction from falling droplets. Appl Sci Res A2:142-154.

[16] Majumdar Alok, LeClair Andre, Hartwig Jason, Martin Adam, Rhys Noah. Numerical modeling of no vent filling of a cryogenic tank. AIAA Joint Propulsion Conference, August 20–24; 2020, AIAA 2020-3797.

[17] Copan J, Balachandar R, Berruti F. Droplet size-velocity characteristics of sprays generated by two phase feed nozzles. Chem Eng Commun 2001;184(1):105–24. https://doi.org/10.1080/009864440108912843.

[18] Luo M, Wu Y, Haidn OJ. Temperature and size measurements of cryogenic spray droplets with globa rainbow refractometry. J Propulsion and Power 2019;35: 359–68.

[19] Malet J, Blumenfeld L, Arndt S, Babic M, Bentaib A, Dabbene F, et al. Sprays in containment: final results of the SARNET spray benchmark. Nucl Eng Des 2011; 241:2162–71.

[20] Mimouni S, Lamy J-S, Lavieville J, Guieu S, Martin M. Modelling of sprays in containment applications with A CMFD code. Nucl Eng Des 2010;240:2260–70.

[21] Ghiaasiaan SM. Two-phase flow, boiling and condensation in conventional and miniature systems. 2nd ed. Cambridge University Press; 2017.

[22] Bejan A. Convection heat transfer. 4th ed. Wiley; 2013.

[23] McAdams WH. Heat transfer. 3rd ed. McGraw-Hill; 1954.

[24] Majumdar A, Juan Valenzuela, LeClair Andre, Moder Jeff. Numerical modeling of self-pressurization and pressure control by a thermodynamic vent system in a cryogenic tank. Cryogenics 2016;74:113–22.